CMS Physics Analysis Summary

Contact: cms-pag-conveners-higgs@cern.ch 2017/05/15

Observation of the SM scalar boson decaying to a pair of τ leptons with the CMS experiment at the LHC

The CMS Collaboration

Abstract

A search for a standard model scalar boson decaying into a pair of τ leptons is performed using events recorded in proton-proton collisions by the CMS experiment at the LHC in 2016. The dataset corresponds to an integrated luminosity of $\sqrt{s} = 13$ TeV at a center-of-mass energy of $\sqrt{s} = 13$ TeV. The τ leptons decay semi-hadronically, or leptonically to an electron or a muon, and the four final states with the largest branching fractions are considered. An excess of events is observed over the expected background prediction with a significance of 4.9 standard deviations for the scalar boson mass $m_H = 125$ GeV, to be compared to an expected significance of 4.7 standard deviations. The best fit of the observed $H \to \tau\tau$ signal cross section times branching fraction for $m_H = 125$ GeV is $1.06^{+0.25}_{-0.24}$ times the standard model expectation.

1 Introduction

In the standard model (SM) of particle physics [1, 2], electroweak symmetry breaking is achieved via the Brout–Englert–Higgs mechanism [3–8], leading to the prediction of the existence of one physical neutral scalar particle, commonly known as the Higgs boson. A particle compatible with such a boson was observed by the ATLAS and CMS experiments at CERN, in the ZZ, $\gamma\gamma$, and WW decay channels [9–11], during the LHC proton-proton (pp) data taking period in 2011 and 2012 at center-of-mass of energies $\sqrt{s} = 7$ and 8 TeV, respectively. Subsequent results from both experiments, summarized in Refs. [12–16], established that the properties of the new particle, including its spin, $\mathcal{CP}$ properties, and measured coupling strengths to SM particles, are consistent with those expected for the SM scalar boson. The mass of the new boson has been determined to be $125.09 \pm 0.21(\text{stat.}) \pm 0.11(\text{syst.})$ GeV based on a combination of ATLAS and CMS measurements [17] using $\gamma\gamma$ and ZZ decay channels.

To establish the mass generation mechanism for fermions, it is necessary to demonstrate the direct coupling of the scalar boson to fermions, and the proportionality of its strength to the fermion mass. The most promising decay channel is $\tau\tau$, because of the large event rate expected in the SM compared to the other leptonic decay modes, and of the smaller contribution from background events with respect to the bb channel.

Searches for a scalar boson decaying to a τ-lepton pair were performed at the LEP [18–21], Tevatron [22, 23], and LHC colliders. Using recent pp collision data at $\sqrt{s} = 7$ and 8 TeV, the ATLAS experiment reported an evidence for scalar bosons decaying into pairs of τ lepton with an observed (expected) significance of 4.5 (3.4) standard deviations (s.d.) for a boson mass of 125 GeV [24]. The CMS Collaboration showed evidence for the same process with an observed (expected) significance of 3.2 (3.7) s.d. [25]. The combination of the results from both experiments yields an observed (expected) significance of 5.5 (5.0) s.d. [26].

This document reports results of a search for the SM scalar boson in pp collisions at a center-of-mass energy of $\sqrt{s} = 13$ TeV, with decays to a pair of τ leptons. The dataset corresponds to an integrated luminosity of 35.9 fb^{-1}, and was collected in 2016. In the following, the symbol ℓ refers to electrons or muons, and the symbol τ_h refers to τ leptons reconstructed in their semi-hadronic decays. The four τ-pair final states with the largest branching fractions are studied in this analysis : $\mu\tau_\text{h}$, eτ_h, $\tau_\text{h}\tau_\text{h}$, and e$\mu$.

2 The CMS detector

The central feature of the CMS apparatus is a superconducting solenoid of 6 m internal diameter, providing a magnetic field of 3.8 T. Within the solenoid volume, there are a silicon pixel and strip tracker, a lead tungstate crystal electromagnetic calorimeter (ECAL), and a brass and scintillator hadron calorimeter (HCAL), each composed of a barrel and two endcap sections. Forward calorimeters extend the pseudorapidity coverage provided by the barrel and endcap detectors. Muons are measured in gas-ionization detectors embedded in the steel flux-return yoke outside the solenoid.

Events of interest are selected using a two-tiered trigger system [27]. The first level (L1), composed of custom hardware processors, uses information from the calorimeters and muon detectors to select events at a rate of around 100 kHz within a time interval of less than 4 μs. The second level, known as the high-level trigger (HLT), consists of a farm of processors running a version of the full event reconstruction software optimized for fast processing, and reduces the event rate to about 1 kHz before data storage.

A more detailed description of the CMS detector, together with a definition of the coordinate system used and the relevant kinematic variables, can be found in Ref. [28].

3 Simulated samples

Signal and background processes are modeled with samples of simulated events. The signal samples with a scalar boson produced through gluon-gluon fusion, vector boson fusion (VBF), or in association with a W or Z boson, are generated with POWHEG 1.0 [29–33]. The MADGRAPH 5.1 [34] generator is used for $Z+$jets and $W+$jets processes, aMC@NLO [35] for diboson production, and POWHEG for $t\bar{t}$ and single-top-quark production. The POWHEG and MADGRAPH generators are interfaced with PYTHIA for parton shower, fragmentation, as well as τ-lepton decays. The PYTHIA parameters affecting the description of the underlying event are set to the CUETP8M1 tune [36]. The various production cross sections and branching fractions for SM processes, including SM scalar boson production, and their corresponding uncertainties are taken from references [37–64]. The $Z/\gamma^* \to \ell\ell/\tau\tau$ sample is corrected for differences to the dilepton mass, $m_{\ell\ell/\tau\tau}$, and dilepton transverse momentum, $p_T(\ell\ell/\tau\tau)$, distributions in observed dimuon events, using an event-by-event reweighting technique.

All generated events are processed through a simulation of the CMS detector based on GEANT4 [65], and are reconstructed with the same algorithms as for data. The simulated samples include additional interactions per bunch crossing, referred to as "pileup". The same distribution of number of concurrent pp collisions in single bunch crossings as observed in the data is reproduced in Monte Carlo (MC) samples by adding minimum bias collision events generated with PYTHIA. The simulated events are weighted such that the pileup distribution matches the data, with an average of about 24 interactions per bunch crossing.

4 Event reconstruction

The reconstruction of observed and simulated events relies on a particle flow (PF) algorithm [66–68], which combines the information from the CMS subdetectors to identify and reconstruct the particles emerging from proton-proton collisions: charged hadrons, neutral hadrons, photons, muons, and electrons. Combinations of these PF objects are then used to reconstruct higher-level objects such as jets, τ_h candidates, or missing transverse energy.

Muons are identified with requirements on the quality of the track reconstruction and on the number of measurements in the tracker and the muon systems [69]. Electrons are identified with a multivariate discriminant combining several quantities describing the track quality, the shape of the energy deposits in the electromagnetic calorimeter, and the compatibility of the measurements from the tracker and the electromagnetic calorimeter [70]. To reject non-prompt or misidentified leptons, a relative lepton isolation is defined as:

$$I^{\ell} \equiv \frac{\sum_{\text{charged}} p_T + \max\left(0, \sum_{\text{neutral}} p_T - \frac{1}{2}\sum_{\text{charged, PU}} p_T\right)}{p_T^{\ell}}. \quad (1)$$

In this expression, $\sum_{\text{charged}} p_T$ is a scalar sum of the transverse momenta of the charged hadrons, electrons, and muons originating from the primary vertex and located in a cone of size $\Delta R = \sqrt{(\Delta\eta)^2 + (\Delta\phi)^2} = 0.4$ (0.3) centered on the muon (electron) direction. The sum $\sum_{\text{neutral}} p_T$ represents the same quantity for neutral particles. The contribution of pileup photons and neutral hadrons is estimated from the scalar sum of the transverse momenta of charged hadrons

originating from pileup vertices in the cone, $\sum_{\text{charged, PU}} p_{\text{T}}$. This sum is multiplied by a factor of 1/2, which corresponds approximately to the ratio of neutral to charged hadron production in the hadronization process of inelastic pp collisions, as estimated from simulation.

Jets are reconstructed with an anti-k_t algorithm implemented in FASTJET [71, 72]. It is based on the clustering of neutral and charged particles within a cone with a distance parameter of 0.4. Charged PF candidates not associated with the primary vertex of the interaction are not considered to build jets. The energy of jets is calibrated based on simulation and observed data through correction factors [73]. In this analysis, jets are required to have p_T greater than 30 GeV and $|\eta|$ less than 4.7, and are separated from the selected leptons by at least $\Delta R = 0.5$.

Semi-hadronically decaying τ leptons, denoted by τ_{h}, are reconstructed with the hadron-plus-strips (HPS) algorithm [74, 75], which is seeded with anti-k_t jets. The HPS algorithm reconstructs τ_{h} candidates based on the number of tracks and on the number of ECAL strips with energy deposits, in the one-prong, one-prong + π^0(s), and three-prong decay modes. A MVA-based discriminator [76], including isolation as well as lifetime information, is used to prevent quark and gluon jets from being identified as τ_{h} candidates. The working point used in this analysis has an efficiency of about 60% for genuine τ_{h}, with about 1% misidentification rate for quark and gluon jets. Electrons and muons misidentified as τ_{h} are suppressed using dedicated criteria based on the consistency between the measurements in the tracker, the calorimeters, and the muon detectors. The working points of the anti-lepton discriminators depend on the final state studied. The τ_{h} energy scale in simulations is corrected per decay mode, based on a measurement in $Z \to \mu\tau_{\text{h}}$ events. The rate and the energy scale of electrons and muons misidentified as τ_{h} are also corrected in MC simulations.

All particles reconstructed in the event are used to determine the missing transverse energy, $\vec{E}_{\text{T}}^{\text{miss}}$. The missing transverse energy is defined as the negative vectorial sum of the transverse momenta of all PF candidates [77]. It is adjusted for the effect of jet energy corrections. Recoil corrections are applied to correct for the mismodeling of $\vec{E}_{\text{T}}^{\text{miss}}$ in the simulated samples of the Drell-Yan, W+Jets and scalar boson production. The corrections are performed on the variable defined as the vectorial difference of the measured missing transverse momentum and total transverse momentum of neutrinos originating from the decay of the vector or scalar bosons.

The visible mass of the di-τ system, m_{vis}, can be used to separate the $\text{H} \to \tau\tau$ signal events from the large contribution of irreducible $\text{Z} \to \tau\tau$ events. However, the neutrinos from the τ-lepton decays take away a large fraction of the τ-lepton energy, and reduce the discriminating power of this variable. The SVFIT algorithm combines the $E_{\text{T}}^{\text{miss}}$ with the four-vectors of both τ candidates, to calculate a more likely estimator of the mass of the parent boson, denoted as $m_{\tau\tau}$. A detailed description of the algorithm can be found elsewhere [78].

5 Event selection

Selected events are classified in the various channels according to the number of selected electrons, muons, and τ_{h} candidates. The resulting event samples are made mutually exclusive by discarding events with additional loosely identified and isolated muons or electrons. Leptons must meet the minimum requirement that the distance of closest approach to the primary vertex satisfies $d_z < 0.2\,\text{cm}$ along the beam direction, and $d_{xy} < 0.045\,\text{cm}$ in the transverse plane. The two leptons assigned to the scalar boson decay are required to have opposite sign electric charges. In the $\mu\tau_{\text{h}}$ channel, events are selected with a combination of triggers that require at least one muon trigger object, or at least one muon and one τ_{h} trigger object, depending on the offline muon p_{T}. In the $\text{e}\tau_{\text{h}}$ channel, the trigger requires at least one electron object, whereas in

the eμ channel, the triggers rely on the presence of both an electron and a muon, which allows for lower online p_T thresholds. In the $\tau_h\tau_h$ channel, the trigger selects events with two loosely isolated τ_h objects.The selection criteria are summarized in Table 1.

Table 1: Kinematic selection requirements for the four di-τ decay channels. The trigger requirement is defined by a combination of trigger objects with p_T over a given threshold, indicated inside parentheses.

Final state	Trigger requirement	Lepton selection		
		p_T (GeV)	η	Isolation
$\mu\tau_h$	$\mu(22)$	$p_T^\mu > 23$	$\lvert\eta^\mu\rvert < 2.1$	$I^\mu < 0.15$
		$p_T^{\tau_h} > 30$	$\lvert\eta^{\tau_h}\rvert < 2.3$	MVA τ_h ID
	$\mu(19)$ & $\tau_h(21)$	$20 < p_T^\mu < 23$	$\lvert\eta^\mu\rvert < 2.1$	$I^\mu < 0.15$
		$p_T^{\tau_h} > 30$	$\lvert\eta^{\tau_h}\rvert < 2.3$	MVA τ_h ID
eτ_h	e(25)	$p_T^e > 26$	$\lvert\eta^e\rvert < 2.1$	$I^e < 0.1$
		$p_T^{\tau_h} > 30$	$\lvert\eta^{\tau_h}\rvert < 2.3$	MVA τ_h ID
$\tau_h\tau_h$	$\tau_h(35)$ & $\tau_h(35)$	$p_T^{\tau_h} > 50$ & 40	$\lvert\eta^{\tau_h}\rvert < 2.1$	MVA τ_h ID
eμ	e(12) & $\mu(23)$	$p_T^e > 13$	$\lvert\eta^e\rvert < 2.5$	$I^e < 0.15$
		$p_T^\mu > 24$	$\lvert\eta^\mu\rvert < 2.4$	$I^\mu < 0.2$
	e(23) & $\mu(8)$	$p_T^e > 24$	$\lvert\eta^e\rvert < 2.5$	$I^e < 0.15$
		$p_T^\mu > 15$	$\lvert\eta^\mu\rvert < 2.4$	$I^\mu < 0.2$

In the $\ell\tau_h$ channels, the W + jets background is reduced by requiring the transverse mass, m_T, to satisfy:

$$m_T \equiv \sqrt{2 p_T^\ell E_T^{miss}(1 - \cos(\Delta\phi))} < 50\,\text{GeV}, \tag{2}$$

where p_T^ℓ is the ℓ transverse momentum and $\Delta\phi$ is the difference in azimuthal angle between the ℓ direction and the $\vec{E}_T^{miss}$.

In the eμ channel, the $t\bar{t}$ background is reduced by requiring $p_\zeta - 0.85 \cdot p_\zeta^{vis} > -35$ or -10 GeV depending on the category, with

$$p_\zeta = \vec{E}_T^{miss} \cdot \vec{\zeta}, \tag{3}$$

$$p_\zeta^{vis} = \vec{p_{T,1}} \cdot \vec{\zeta} + \vec{p_{T,2}} \cdot \vec{\zeta}, \tag{4}$$

where $\vec{\zeta}$ is a unit vector along the bisector of the directions of the leptons in the transverse plane, and $p_{T,1}$ and $p_{T,2}$ are the transverse momenta of the two leptons. In addition, events with a b-tagged jet are discarded to further suppress the $t\bar{t}$ background in the eμ channel.

6 Categorization

The event sample is split into three mutually exclusive categories per final state, according to the number of reconstructed jets. In each category the two variables that yield the best sensitivity to the signal are chosen to build two-dimensional distributions.

The three categories are defined as:

- **0 jet**: This category targets scalar boson events produced via gluon-gluon fusion. The two variables chosen to extract the results are m_{vis}, and the reconstructed τ_h candidate decay mode (in the $\mu\tau_h$ and eτ_h final states) or the p_T of the muon (in the eμ channel). In the one-prong and one-prong + π^0(s) τ_h decay modes in the $\mu\tau_h$

and $e\tau_h$ channels, $Z \to \ell\ell$ is a dominant background, together with $Z \to \tau\tau$. The m_{vis} variable is chosen over $m_{\tau\tau}$ because it separates the signal from the $Z \to \ell\ell$ background, which peaks around the Z boson mass. The $Z \to \ell\ell$ background is negligible for τ_h reconstructed in the 3-prong decay mode. The two-dimensional distributions for the signal and $Z \to \ell\ell$ background in the 0 jet category of the $\mu\tau_h$ final state are shown in Fig. 1. In the $\tau_h\tau_h$ final state, only one dimension, $m_{\tau\tau}$, is considered because of the low event yields due to relatively high τ_h p_T thresholds at trigger level, and because of the shraply falling τ_h p_T distribution.

- **VBF**: This category targets scalar boson events produced via VBF. Events are selected with at least two (exactly two) jets with $p_T > 30$ GeV in the $\mu\tau_h$, $e\tau_h$, and $\tau_h\tau_h$ ($e\mu$) channels. In the $\mu\tau_h$, $e\tau_h$, and $e\mu$ channels, the two leading jets are required to have an invariant mass, m_{jj}, larger than 300 GeV. The variable $p_T^{\tau\tau}$, defined as the vectorial sum of the reconstructed visible τ leptons and E_T^{miss}, is required to be greater than 50 (100) GeV in the $\mu\tau_h$ and $e\tau_h$ ($\tau_h\tau_h$) channels to reduce the contribution from QCD mutijet and W+jets backgrounds. In addition the p_T threshold to the τ_h candidate is raised to 40 GeV in the $\mu\tau_h$ channel, and the two leading jets in the $\tau_h\tau_h$ channel should be separated by at least $\Delta\eta = 2.5$. The two observables in the VBF category are $m_{\tau\tau}$ and m_{jj}. The two-dimensional distributions for the signal and $Z \to \tau\tau$ background in the VBF category of the $\mu\tau_h$ final state are shown in Fig. 1.

- **Boosted**: This category contains all other events that do not enter one of the previous categories, namely events with one jet and events with several jets that fail the specific requirements of the VBF category. It contains gluon-gluon fusion events produced in association with one or more jets, VBF events where one of the jets has escaped detection or with low m_{jj}, as well as scalar bosons produced in association with a W or a Z boson decaying hadronically. While $m_{\tau\tau}$ is chosen as one of the dimensions of the distributions, $p_T^{\tau\tau}$ is taken as the second dimension to specifically target ggH events with a boosted boson recoiling against jets. Most background processes, including W+jets and QCD multijet, typically have low $p_T^{\tau\tau}$. The two-dimensional distributions for the signal and W+jets background in the boosted category of the $\mu\tau_h$ final state are shown in Fig. 1.

The categories and the variables used for two dimensional distributions are summarized in Table 2.

7 Background estimation

The largest irreducible source of background is the Drell–Yan production of $Z/\gamma^* \to \tau\tau, \ell\ell$. The corresponding MC sample is split, based on matching between objects at the generator and at the detector levels, into events with prompt leptons (muons or electrons), hadronic decays from τ leptons, and jets or misidentified objects at the detector level that do not have corresponding objects at generator level within $\Delta R < 0.2$. To constrain the yield of the $Z \to \tau\tau, \ell\ell$ events, a dedicated control sample of $Z \to \mu\mu$ events is collected in data with a single muon trigger, and compared to simulation. It is built by requiring two well identified and isolated opposite-sign muons with p_T greater than 25 GeV, with an invariant mass between 70 and 110 GeV. Events with additional isolated muons or electrons are rejected. The purity of this sample exceeds 99% and allows to correct simulations to better reproduce the Drell–Yan process in data. A reweighting based on $m_{\ell\ell/\tau\tau}$, $p_T(\ell\ell/\tau\tau)$, and m_{jj}, is applied to reproduce the kinemat-

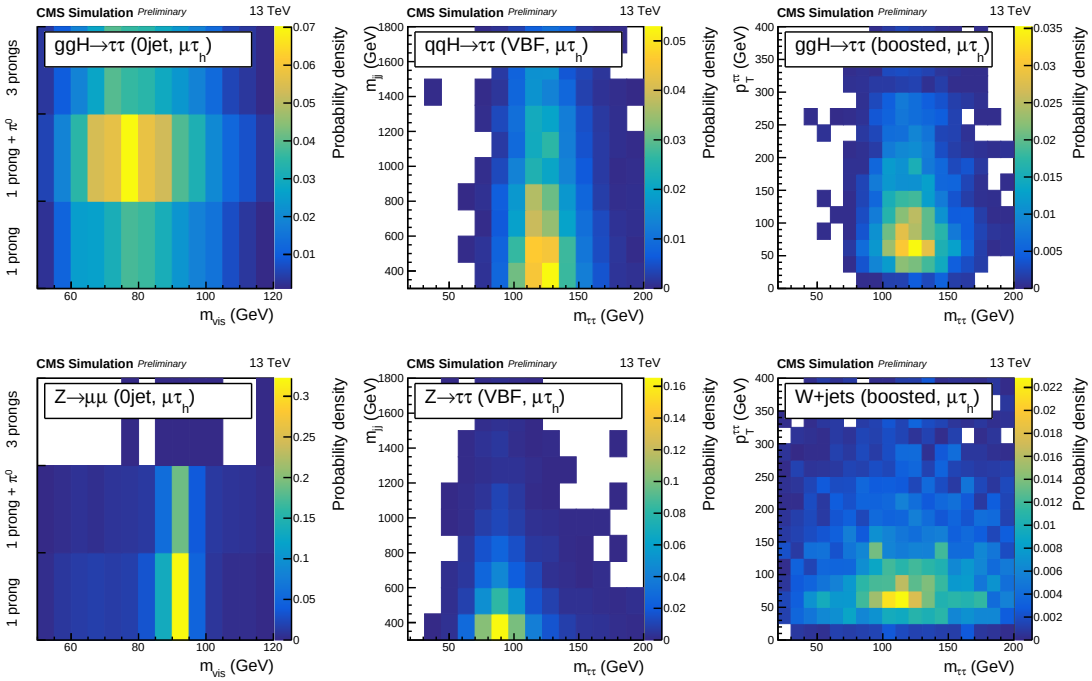

Figure 1: Distributions for the signal (top) and typical background processes (bottom) of the two observables chosen in the 0 jet (left), VBF (center), and boosted (right) categories in the $\mu\tau_h$ final state. The $Z \to \mu\mu$ background in the 0 jet category is concentrated in the regions where the visible mass is close to 90 GeV and is negligible when the reconstructed τ_h decay mode is 3-prongs. The $Z \to \tau\tau$ background in the VBF category mostly lies at low m_{jj} values whereas the distribution of VBF signal events extends to high m_{jj} values. In the boosted category, the W+jets background, which behaves similarly as the QCD background, is rather flat with respect to $m_{\tau\tau}$, and is concentrated at low $p_T^{\tau\tau}$ values.

Table 2: Category selection and variables used to build the two dimensional kinematical distributions. The events not selected in the 0-jet nor VBF category are included in the boosted category.

	Selection		
	0-jet	VBF	Boosted
$e\mu$	No jet	2 jets, $m_{jj} > 300\,\text{GeV}$	Others
$\mu\tau_h$	No jet	≥ 2 jets, $m_{jj} > 300\,\text{GeV}$, $p_T^{\tau\tau} > 50\,\text{GeV}$, $p_T^{\tau_h} > 40\,\text{GeV}$	Others
$e\tau_h$	No jet	≥ 2 jets, $m_{jj} > 300\,\text{GeV}$, $p_T^{\tau\tau} > 50\,\text{GeV}$	Others
$\tau_h\tau_h$	No jet	≥ 2 jets, $p_T^{\tau\tau} > 100\,\text{GeV}$, $\Delta\eta_{jj} > 2.5$	Others
	Variables		
$e\mu$	p_T^{μ}, m_{vis}	m_{jj}, $m_{\tau\tau}$	$p_T^{\tau\tau}$, $m_{\tau\tau}$
$\mu\tau_h$	τ_h decay mode, m_{vis}	m_{jj}, $m_{\tau\tau}$	$p_T^{\tau\tau}$, $m_{\tau\tau}$
$e\tau_h$	τ_h decay mode, m_{vis}	m_{jj}, $m_{\tau\tau}$	$p_T^{\tau\tau}$, $m_{\tau\tau}$
$\tau_h\tau_h$	$m_{\tau\tau}$	m_{jj}, $m_{\tau\tau}$	$p_T^{\tau\tau}$, $m_{\tau\tau}$

ics of observed events. The electroweak production of Z bosons is also taken into account in the analysis; it contributes mostly to the VBF category.

The background from W + jets production contributes significantly to the $e\tau_h$ and $\mu\tau_h$ channels when the W boson decays leptonically and a jet is misidentified as a τ_h. The W + jets distribution is modelled using simulation, while its yield is estimated using data, as explained below. The simulated sample is normalized based on the agreement between observed data and predicted backgrounds in a W+jets-enriched control region that is obtained by applying all selection criteria, with the exception that m_T is required to be greater than 80 GeV. In each category, the W + jets background yield in a high-m_T region is normalized to the observed yield. The W + jets purity in this region varies from about 50% in the boosted category to 85% in the 0-jet category. The extrapolation factor to the low-m_T signal region is obtained from the simulation. The uncertainty in the W + jets yield resulting from this procedure is between 10 and 30% depending on the event category. In practice the high-m_T sidebands are considered as control regions in the fit used to extract the results in order to treat correctly the correlations with the uncertainties in the signal region. These control regions are shown in Fig. 2. The constraints obtained in the boosted category are extrapolated to the VBF category of the corresponding final state because the topology between boosted and VBF events is similar, and the VBF category is statistically limited. In the $e\mu$ and $\tau_h\tau_h$ final states, the W + jets background is small compared to other backgrounds, and its contribution is entirely estimated from MC simulations.

The $t\bar{t}$ production process is one of the main backgrounds in the $e\mu$ channel. The two-dimensional distributions in all final states are predicted by simulation, and the yield is adjusted to the one observed in a $t\bar{t}$-enriched sample orthogonal to the signal region. The control region, shown in Fig. 2, is defined similarly as the $e\mu$ signal region, except that the p_ζ requirement is inverted and the events should contain at least one jet.

QCD multijet events constitute another important source of reducible background in the $\ell\tau_h$ channels. The QCD multijet background yield is extracted using a sample where the ℓ and the τ_h candidates have same-sign charge. In this sample, the QCD multijet yield is obtained by subtracting from the data the contribution of the Drell–Yan, $t\bar{t}$, diboson, and W + jets processes, estimated as explained above. This QCD multijet yield is then rescaled to account for differences between the composition in the same-sign and opposite-sign regions. The scaling factors are extracted from QCD multijet enriched control regions, composed of events with the ℓ and τ_h candidates satisfying relaxed isolation requirement. The constraints obtained from the boosted control regions are extrapolated to the boosted and VBF categories of the signal region, because the event topologies are similar and the VBF control regions have lower purity and are statistically limited. These control regions are shown in Fig. 2. The same technique is used in the $e\mu$ final state, but no control region is included in the fit because QCD multijet events contribute little to the total background in this final state.

In the $\tau_h\tau_h$ channel, the large QCD multijet background is estimated with a different method, from a sample composed of events with opposite-sign τ_h satisfying relaxed isolation requirement, disjoint from the signal region. In this region, the QCD multijet background shape and yield are obtained by subtracting from the observed data the contribution of the Drell–Yan, $t\bar{t}$, and W + jets processes, estimated as explained above. The QCD multijet background yield in the signal region is obtained by multiplying the yield in the control region by an extrapolation factor. The extrapolation factor is measured in events passing similar selection criteria as those in the signal region, and in the relaxed isolation region, except that the τ_h candidates are required to have the same electric charge. The events selected with the relaxed isolation re-

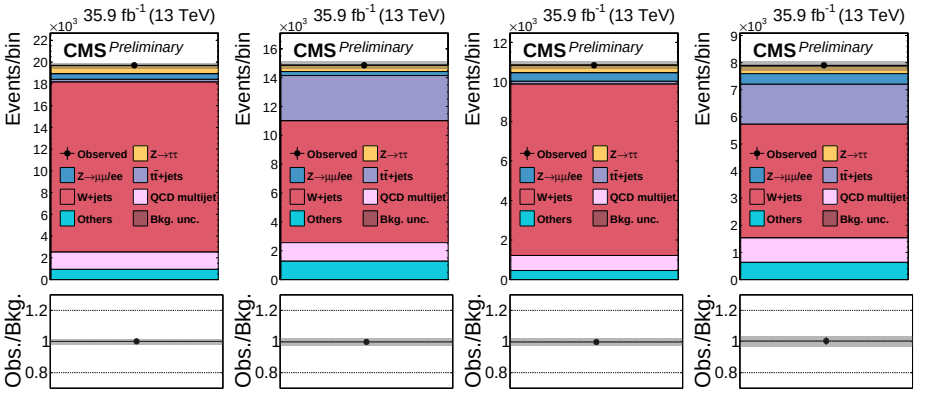

(a) $\mu\tau_h$, 0 jet (b) $\mu\tau_h$, boosted (c) $e\tau_h$, 0 jet (d) $e\tau_h$, boosted

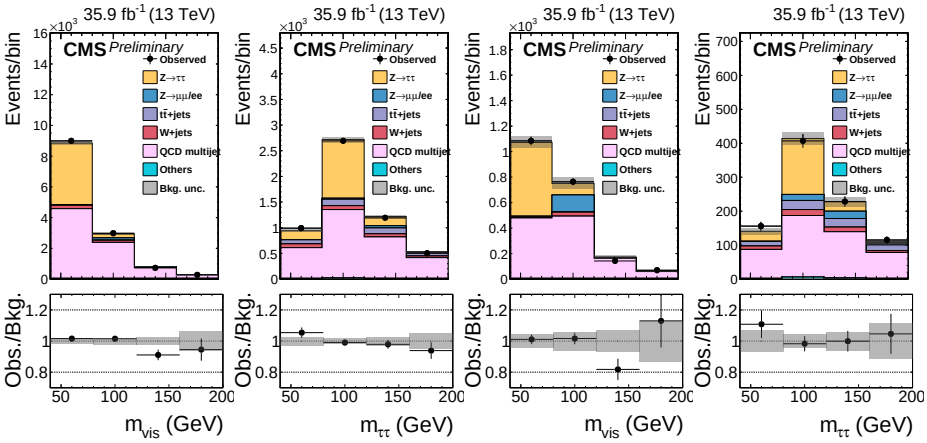

(e) $\mu\tau_h$, 0 jet (f) $\mu\tau_h$, boosted (g) $e\tau_h$, 0 jet (h) $e\tau_h$, boosted

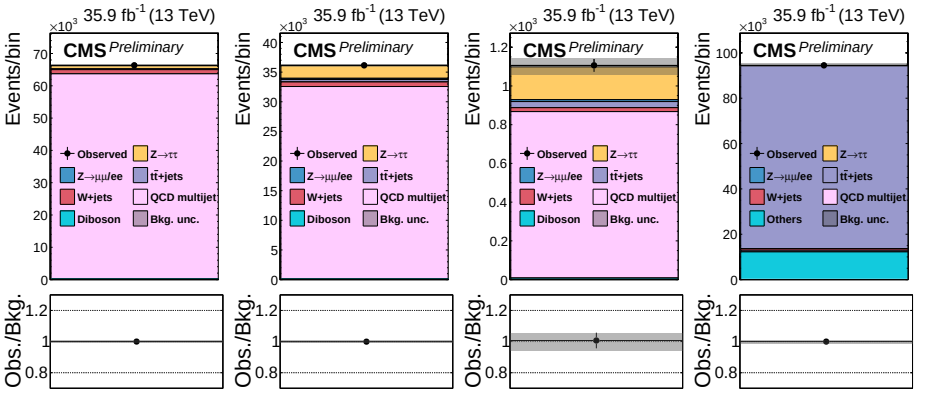

(i) $\tau_h\tau_h$, 0 jet (j) $\tau_h\tau_h$, boosted (k) $\tau_h\tau_h$, VBF (l) $e\mu$, ≥ 1 jet

Figure 2: Signal-free control regions used in the maximum likelihood fit, together with the signal regions, to extract the results. These regions control the yields of the W+jets (a,b,c,d), QCD multijet (e,f,g,h,i,j,k), and $t\bar{t}$ (l) backgrounds, in the $\mu\tau_h$ (a,b,e,f), $e\tau_h$ (c,d,g,h), $\tau_h\tau_h$ (i,j,k) or $e\mu$ (l) final states. The constraint on the $t\bar{t}$ background is obtained in the $e\mu$ final state, but propagated to all final states. The constraints on the W+jets and QCD multijet backgrounds obtained in the boosted categories of the $\mu\tau_h$ and $e\tau_h$ final states are propagated to the VBF categories of these final states.

quirement form control regions in the fit used to extract the results, which are shown in Fig. 2.

The small contributions from diboson and single-top-quark production are estimated from simulation. The background H $\to$ WW is estimated from simulation

8 Systematic uncertainties

8.1 Uncertainties related to object reconstruction and identification

The τ_h reconstruction is the source of dominant experimental uncertainties. The τ_h identification efficiencies for genuine τ_h leptons sum up to an overall rate uncertainty of 5%. This number is partially uncorrelated among di-τ channels because the τ_h candidates are required to pass different working points of the anti-lepton discriminators. The trigger efficiency uncertainty per τ_h leg amounts to an additional 5%, which leads to a total of 10% uncertainty for processes estimated from MC simulations in the $\tau_h\tau_h$ final state.

An uncertainty of 1.2% for the visible energy scale of genuine τ_h leptons affects both the distributions and the yields of signal and background processes. It is uncorrelated among the 1 prong, 1 prong + π^0, and 3 prong decay modes. The magnitude of the uncertainty was determined in $Z \to \mu\tau_h$ events with a tag-and-probe measurement. Among these events, less than half overlap with the events selected in the $\mu\tau_h$ channel of this analysis. The present analysis constrains the visible τ_h energy scale uncertainty to about 0.3%. This decrease in the size of the uncertainty is explained by the addition of two other final states with τ_h candidates (eτ_h and $\tau_h\tau_h$), by the higher number of events in the MC simulations, and by the finer categorization that leads to regions with a large $Z \to \tau\tau$ purity. Even in the most boosted categories, the reconstructed τ_h typically have moderate p_T ($p_T < 100$ GeV) and are reconstructed in the barrel of the detector. As tracks are well measured by the CMS detector for this range of p_T, the visible energy scale of genuine τ_h leptons is fully correlated for all τ_h leptons considered in the analysis, irrespective of their p_T and η.

In the 0-jet category of the eτ_h and $\mu\tau_h$ channels, the relative contribution of τ_h in a given reconstructed decay mode is allowed to fluctuate by 3% to account for possibly different reconstruction and identification efficiencies. The effect of decay mode migration is negligible in other categories, where all reconstructed decay modes are treated together.

For events where muons or electrons are misidentified as τ_h, essentially $Z \to$ ee events in the eτ_h final state and $Z \to \mu\mu$ events in the $\mu\tau_h$ final state, the τ_h identification leads to prefit rate uncertainties between 12 and 25% per reconstructed τ_h decay mode. Using m_{vis} and the reconstructed τ_h decay mode as the two dimensions in the 0 jet category of the $\mu\tau_h$ and eτ_h channels, helps in reducing the uncertainty after the signal extraction fit: the uncertainty in the rate of muons or electrons misidentified as τ_h becomes of the order of 5%. The energy scale uncertainty for muons or electrons misidentified as τ_h is 1.5 or 3%, respectively, and is uncorrelated between reconstructed τ_h decay modes. The fit constrains these uncertainties to about one third of their initial values. For events where quark or gluon jets are misidentified as τ_h, an uncertainty of 20% per step of 100 GeV τ_h p_T accounts for potential MC mismodeling of the jet$\to \tau_h$ misidentification rate as a function of the τ_h p_T.

In the decay channels with muons or electrons, the uncertainties in the muon and electron identification, isolation, and trigger efficiencies lead to rate uncertainties of 2% for muons, and 2% for electrons. The uncertainty in the electron energy scale, which amounts to 2.5% in the endcaps and 1% in the barrel of the detector, is relevant only in the eμ final state, where it affects the final distributions. In the eτ_h channel the electron energy scale uncertainty is negligible

compared to the τ_h energy scale uncertainty. In all channels, the effect of the uncertainty in the muon energy scale is negligible.

The E_T^{miss} scale uncertainties [77], which are computed event-by-event, affect the event distributions through the event selection, and are propagated through the di-τ mass reconstruction. The unclustered E_T^{miss} scale uncertainties come from four independent sources related to the CMS subdetectors: tracker, ECAL, HCAL, and HCAL forward. The clustered E_T^{miss} scale uncertainties are related to uncertainties in the jet energy scale measurement, which lead to uncertainties in the E_T^{miss} calculation. The E_T^{miss} scale uncertainties are among the most impactful nuisances in the analysis, together with the visible τ_h energy scale uncertainties.

The uncertainties in the jet energy scale depend on the jet p_T and jet η [73]. The 27 independent sources of jet energy scale uncertainty are considered as uncorrelated, and are propagated to the computation of the number of jets, which affects the repartition of events between the 0 jet, VBF, and boosted categories, and to the computation of m_{jj}, which is one of the observables in the VBF category.

The uncertainty related to discarding events with a b-tagged jet in the eμ final state amounts to up to 5% for the $t\bar{t}$ background. The uncertainty in the mis-tagging rate of gluon and light flavor jets is negligible.

8.2 Background estimation uncertainties

A $t\bar{t}$-enriched region, obatined in the eμ channel, is added to the maximum likelihood fit in order to control the normalization of this process in the signal region. The uncertainty from the fit in the control region is automatically propagated to the signal region for all final states. The resulting uncertainty is of the order of 5%.

The $Z \to \tau\tau$ background yield and distribution are corrected as a function of $p_T(\ell\ell)$, $m_{\ell\ell}$, and m_{jj}, based on the agreement between data and background prediction in a $Z \to \mu\mu$-enriched region. The extrapolation uncertainty related to kinematic differences in the selections in both regions range between 3 and 10% depending on the category. In addition, shape uncertainties related to the uncertainties in the applied corrections are considered. These uncertainties can reach 20% for some ranges of m_{jj} in the VBF category.

The uncertainties in the W + jets event yields, in the case of the eτ_h and $\mu\tau_h$ final states, are derived through the inclusion of dedicated control regions in the fit. They account for the statistical limitation of observed data, the statistical limitation of the W + jets simulation sample, and the systematic uncertainties of other processes in the control regions. An uncertainty in the extrapolation of the constraints from the high-m_T control regions to the low-m_T signal regions, is additionaly taken into account. The latter ranges from 5 to 10%, and is obtained by comparing the agreement of the m_T distributions of simulated and observed $Z \to \mu\mu$ events where one of the muons is replaced by E_T^{miss} to mimic W+jets events, after mutliplying the mass of the reconstructed parent boson in the rest frame by the ratio of the W boson mass to the Z boson mass. In the eμ and τ_h channels, where the W+jets background is entirely estimated from simulation, the uncertainty in the yield of this small background is equal to 20%.

The uncertainty in the QCD multijet background yield in the eμ final state ranges from 10 to 20%, depending on the category. It corresponds to the uncertainty in the extrapolation factor from the same-sign to opposite-sign region. In the eτ_h and $\mu\tau_h$ final states, uncertainties from the fit of the control regions with leptons passing relaxed isolation conditions are considered together with a 20% uncertainty that accounts for the extrapolation from the relaxed isolation region to the isolated signal region. In the $\tau_h\tau_h$ final state, an uncertainty that ranges from

3 to 15% accounts for limited non-closures in dedicated control regions. It adds up to the uncertainty extracted from fitting the control region with τ_h passing relaxed isolation criteria described previously.

The combined systematic uncertainty in the background yield arising from diboson and single-top-quark production processes is estimated to be 5% based on recent CMS measurements.

8.3 Signal prediction uncertainties

The rate and acceptance uncertainties for the signal processes related to the theoretical calculations are due to uncertainties in the parton distribution functions (PDF), variations of the renormalization and factorization scales, and uncertainties in the modelling of the underlying event and parton showers (UEPS). The magnitude of the rate uncertainty depends on the production process and on the event category.

The inclusive uncertainty related to the PDF amounts to 3.2, 2.1, 1.9, and 1.6%, respectively, for the ggH, VBF, WH, and ZH production modes. The corresponidng uncertainty for the variation of the renormalization and factorization scales is 3.9, 0.4, 0.7, and 3.8%, respectively. The acceptance uncertainties related to the particular selection criteria used in this analysis are less than 1% for the ggH and qqH productions for the PDF uncertainties. The acceptance uncertainties for the qqH production for the QCD scale uncertainties are also less than 1%, while the corresponding uncertainties for the ggH process are treated as shape uncertainties as the uncertainty increases linearly with $p_T^{\tau\tau}$ and m_{jj}.

The p_T distribution of the scalar boson in the POWHEG 2.0 simulations is tuned to match the NNLO plus next-to-next-to-leading-logarithmic (NNLL) prediction from HRES2.1 [79, 80]. The acceptance changes with the variation of the parton shower tune in Herwig samples are considered as additional uncertainties, and amount to up to 7% in the boosted category. The theoretical uncertainty on the branching fraction of the scalar boson to τ leptons is equal to 2.1%.

8.4 Other uncertainties

The uncertainty in the integrated luminosity amounts to 2.5% for data collected in 2016; this affects the normalization of processes fully estimated through MC simulations.

Uncertainties related to the finite number of simulated events, or to the limited number of events in data control regions, in every bin of the distributions used to extract the results, are taken into account. They are uncorrelated across different samples, and across bins of a single distribution. The combined effect of these bin uncertainties has a large impact on the precision of the analysis, especially in the VBF category where the background templates are less populated than in the other categories.

The systematic uncertainties considered in the analysis are summarized in Table 3.

9 Results

The search for an excess of SM scalar boson events over the expected background involves a global maximum likelihood fit based on two-dimensional distributions in all channels, together with control regions for the $t\bar{t}$, QCD multijet, and W+jets backgrounds.

Figures 3-14 show the distributions observed in all channels and categories of this analysis, together with the expected background and signal distributions. The signal prediction for a scalar

Table 3: Sources of systematic uncertainties, and their magnitudes. If the global fit to the signal and control regions, described in the next section, significantly constrains these uncertainties, their post-fit values are indicated in the third column.

Source of uncertainty	Magnitude	
	Prefit	Postfit
τ_h energy scale	1.2% on energy scale	0.2-0.3%
e energy scale	1-2.5% on energy scale	0.2-0.5%
e misidentified as τ_h energy scale	3% on energy scale	0.6-0.8%
μ misidentified as τ_h energy scale	1.5% on energy scale	0.3-1.0%
Jet energy scale	27 sources, event-by-event	-
E_T^{miss} energy scale	Event-by-event	-
τ_h ID & isolation	5% per τ_h	3.5%
τ_h trigger	5% per τ_h	3%
τ_h reconstruction per decay mode	3% migration between decay modes	2%
e ID & isolation & trigger	2%	-
μ ID & isolation & trigger	2%	-
e misidentified as τ_h rate	12% per τ_h decay mode	5%
μ misidentified as τ_h rate	25% per τ_h decay mode	3-8%
Jet misidentified as τ_h rate	20% per 100 GeV τ_h p_T	15%
$Z \to \tau\tau/\ell\ell$ estimation	Normalization: 7-15%	3-15%
	Uncertainty on $m_{\ell\ell/\tau\tau}$, $p_T(\ell\ell/\tau\tau)$, and m_{jj} corrections	-
W + jets estimation	Normalization, eμ and $\tau_h\tau_h$: 4-20%	-
	Extrap. from high-m_T region, eτ_h and $\mu\tau_h$: 5-10%	-
	Unc. from CR, eτ_h and $\mu\tau_h$: $\simeq 5-15\%$	-
QCD multijet estimation	Normalization, eμ: 10-20%	5-20%
	Unc. from CR, eτ_h, $\tau_h\tau_h$, and $\mu\tau_h$: $\simeq 5-15\%$	-
	Extrap. from anti-iso. region, eτ_h and $\mu\tau_h$: 20%	7-10%
	Extrap. from anti-iso. region, $\tau_h\tau_h$: 3-15%	3-10%
Diboson normalization	5%	-
Single-top normalization	5%	-
$t\bar{t}$ estimation	Normalization from CR: $\simeq$ 5%	-
	Uncertainty on top quark p_T reweighting	-
Luminosity	2.5%	-
b-tagged jet veto (eμ)	3.5-5.0%	-
Limited number of events	Statistical uncertainty in every bin	-
Signal theoretical uncertainty	Up to 20%	-

boson with $m_H = 125\,GeV$ is normalized to its best-fit cross section times branching fraction. The background distributions are adjusted to the results of the global maximum likelihood fit.

The distributions of the final discriminating variable obtained for each category and each channel as two-dimensional distributions, and the control regions, are combined in a binned likelihood, involving the expected and observed numbers of events in each bin. The expected number of signal events is the one predicted by the SM for the production of a scalar boson of mass m_H decaying into a pair of τ leptons, multiplied by a signal strength modifier μ treated as free parameter in the fit.

The systematic uncertainties are represented by nuisance parameters that are varied in the

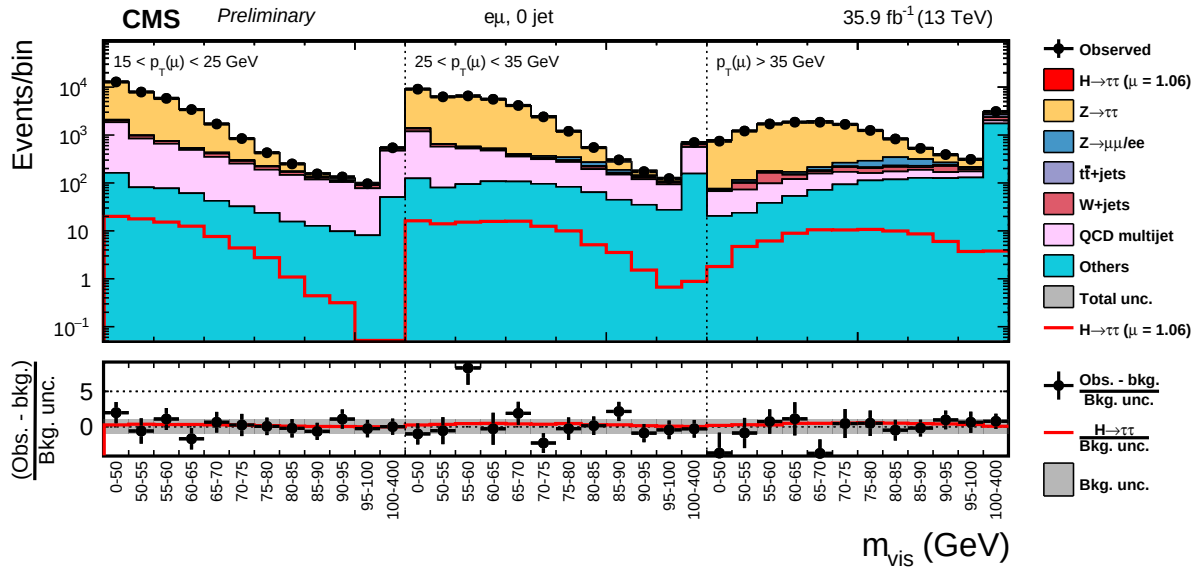

Figure 3: Observed and predicted 2D distributions in the 0-jet category of the eμ final state. The normalization of the predicted background distributions corresponds to the result of the global fit. The signal distribution is normalized to its best-fit signal strength. The background histograms are stacked. The "others" background contribution includes events from diboson and single-top-quark production, as well as scalar boson decays to a pair of W bosons. The background uncertainty band accounts for all sources of background uncertainties, systematic as well as statistical, after the global fit.

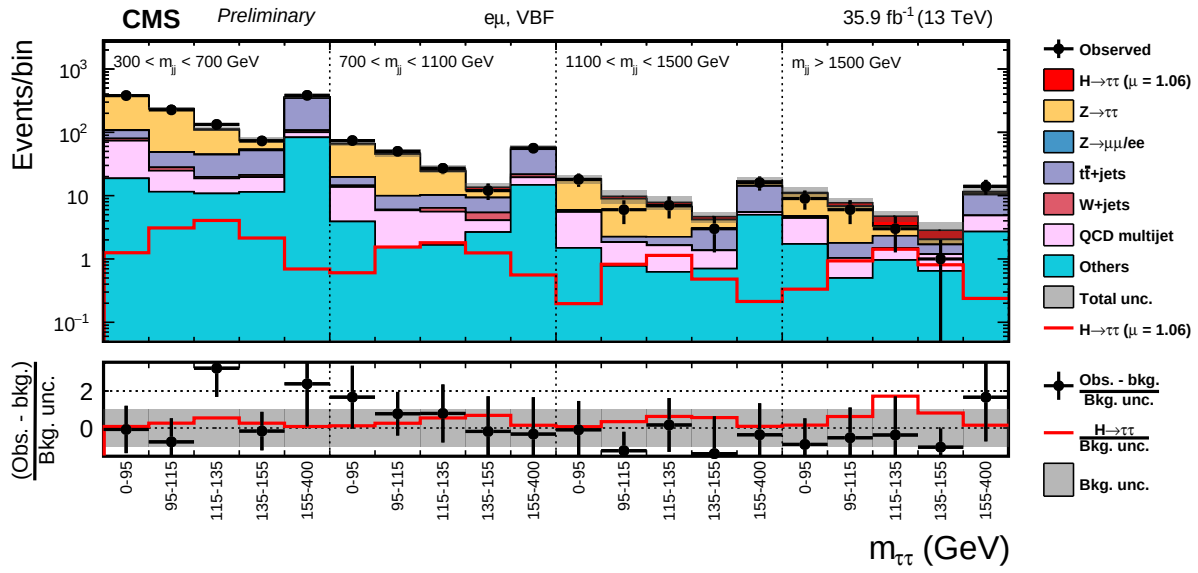

Figure 4: Observed and predicted 2D distributions in the VBF category of the eμ final state. The normalization of the predicted background distributions corresponds to the result of the global fit. The signal distribution is normalized to its best-fit signal strength. The background histograms are stacked. The "others" background contribution includes events from diboson and single-top-quark production, as well as scalar boson decays to a pair of W bosons. The background uncertainty band accounts for all sources of background uncertainties, systematic as well as statistical, after the global fit.

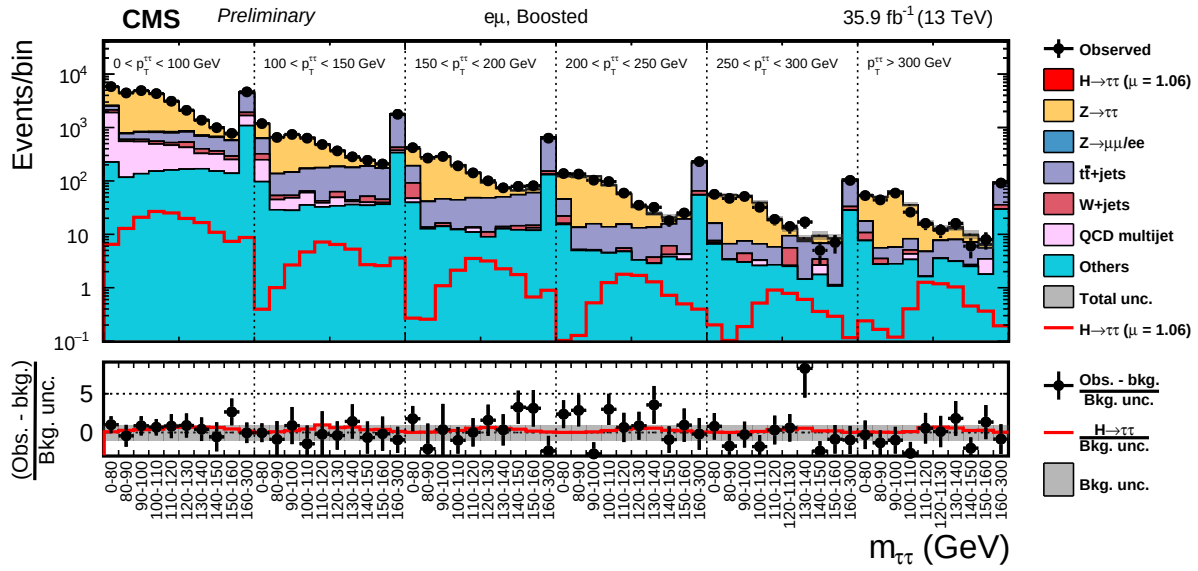

Figure 5: Observed and predicted 2D distributions in the boosted category of the eμ final state. The normalization of the predicted background distributions corresponds to the result of the global fit. The signal distribution is normalized to its best-fit signal strength. The background histograms are stacked. The "others" background contribution includes events from diboson and single-top-quark production, as well as scalar boson decays to a pair of W bosons. The background uncertainty band accounts for all sources of background uncertainties, systematic as well as statistical, after the global fit.

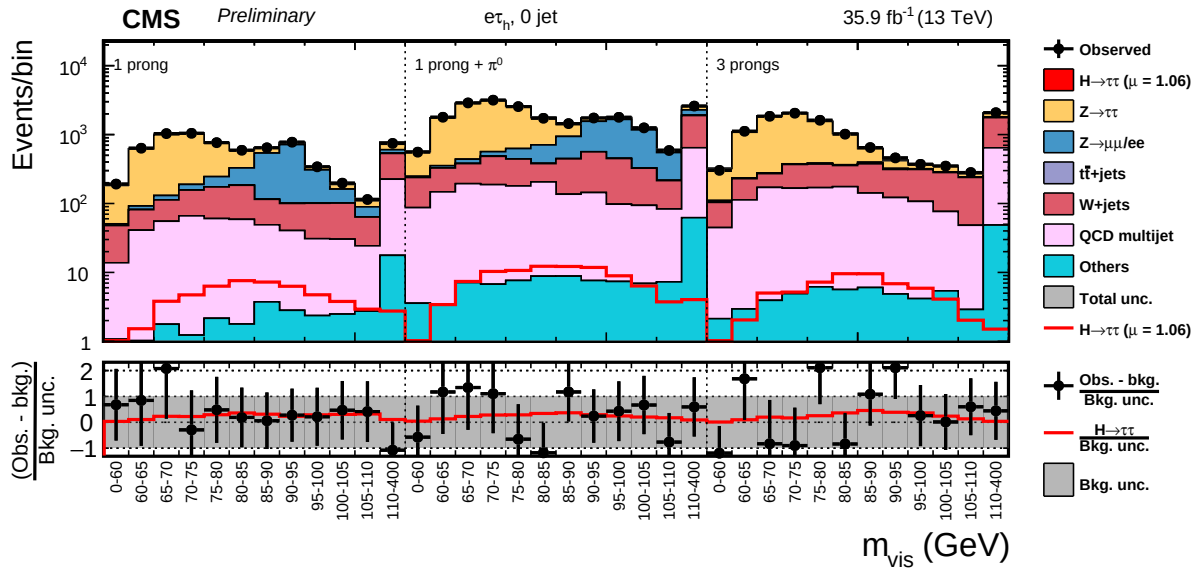

Figure 6: Observed and predicted 2D distributions in the 0-jet category of the eτ_h final state. The normalization of the predicted background distributions corresponds to the result of the global fit. The signal distribution is normalized to its best-fit signal strength. The background histograms are stacked. The "others" background contribution includes events from diboson and single-top-quark production, as well as scalar boson decays to a pair of W bosons. The background uncertainty band accounts for all sources of background uncertainties, systematic as well as statistical, after the global fit.

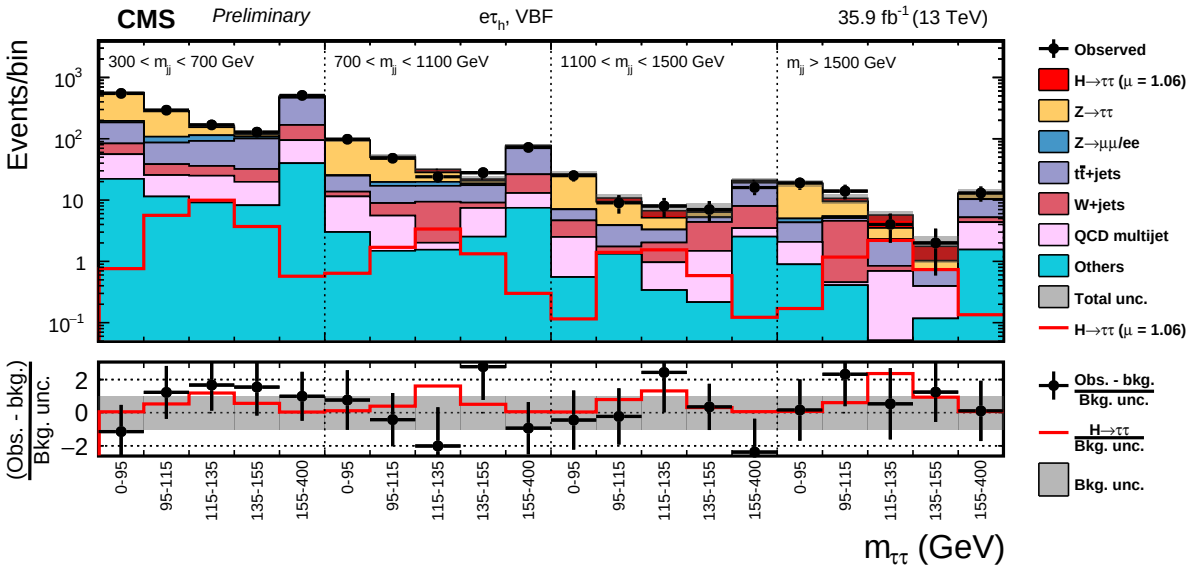

Figure 7: Observed and predicted 2D distributions in the VBF category of the eτ_h final state. The normalization of the predicted background distributions corresponds to the result of the global fit. The signal distribution is normalized to its best-fit signal strength. The background histograms are stacked. The "others" background contribution includes events from diboson and single-top-quark production, as well as scalar boson decays to a pair of W bosons. The background uncertainty band accounts for all sources of background uncertainties, systematic as well as statistical, after the global fit.

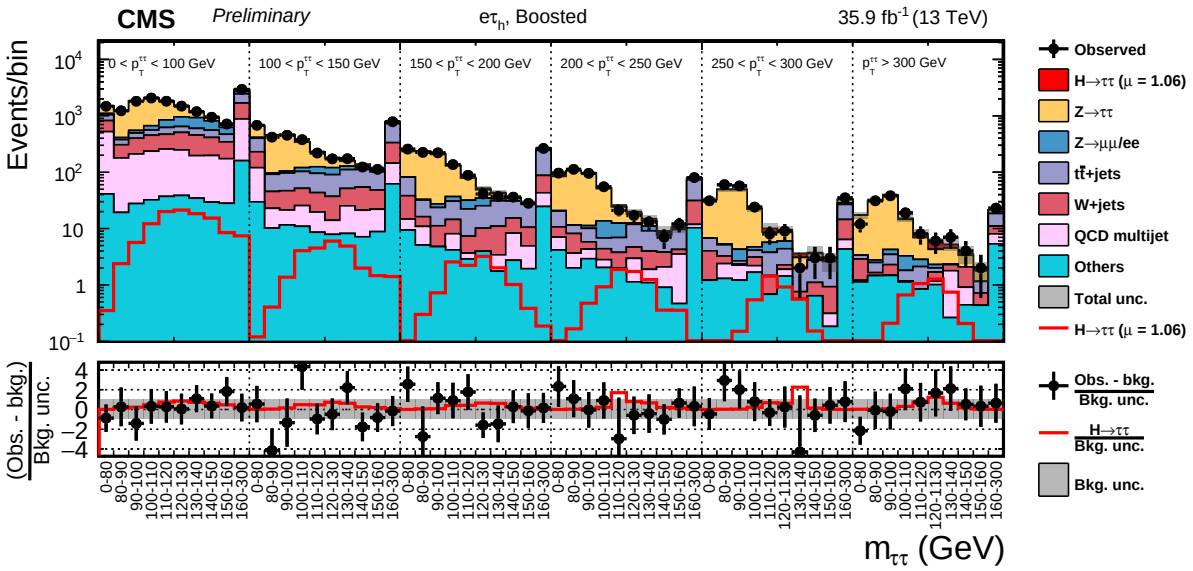

Figure 8: Observed and predicted 2D distributions in the boosted category of the eτ_h final state. The normalization of the predicted background distributions corresponds to the result of the global fit. The signal distribution is normalized to its best-fit signal strength. The background histograms are stacked. The "others" background contribution includes events from diboson and single-top-quark production, as well as scalar boson decays to a pair of W bosons. The background uncertainty band accounts for all sources of background uncertainties, systematic as well as statistical, after the global fit.

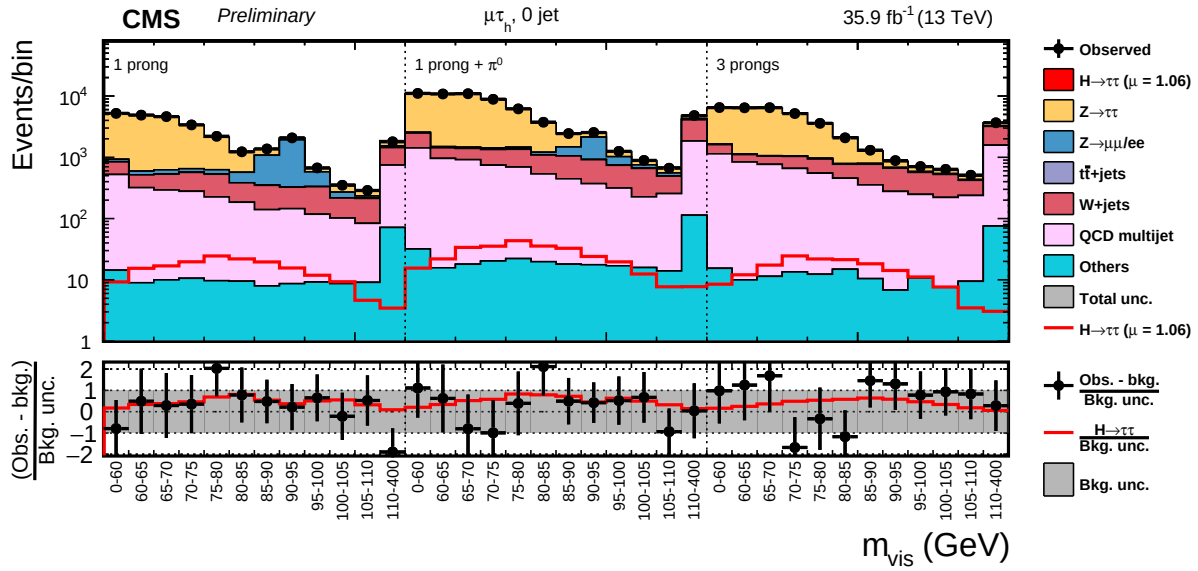

Figure 9: Observed and predicted 2D distributions in the 0-jet category of the $\mu\tau_h$ final state. The normalization of the predicted background distributions corresponds to the result of the global fit. The signal distribution is normalized to its best-fit signal strength. The background histograms are stacked. The "others" background contribution includes events from diboson and single-top-quark production, as well as scalar boson decays to a pair of W bosons. The background uncertainty band accounts for all sources of background uncertainties, systematic as well as statistical, after the global fit.

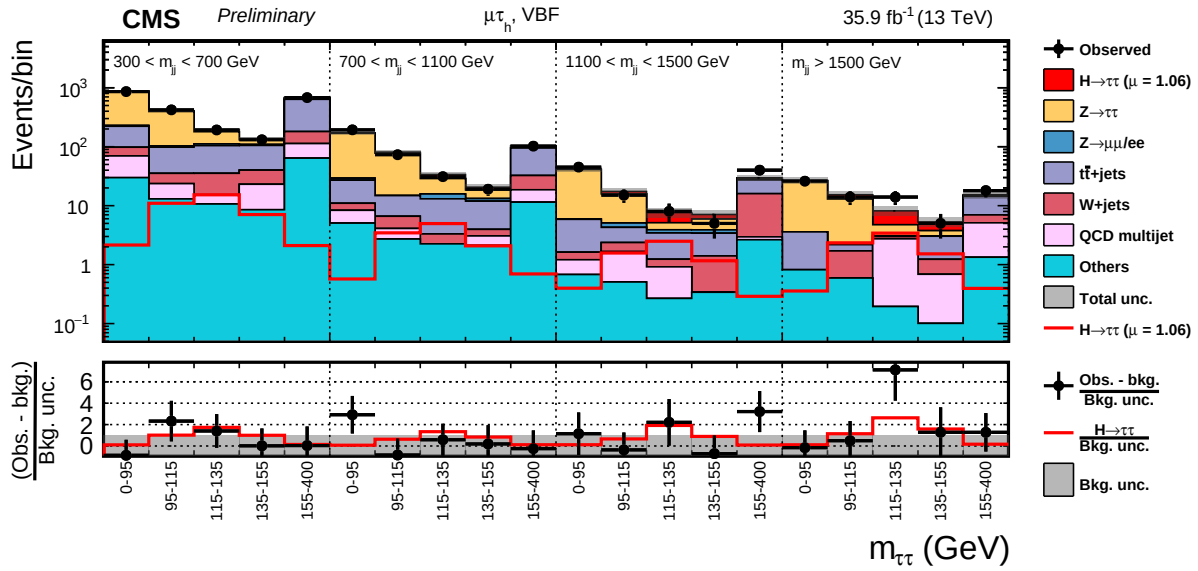

Figure 10: Observed and predicted 2D distributions in the VBF category of the $\mu\tau_h$ final state. The normalization of the predicted background distributions corresponds to the result of the global fit. The signal distribution is normalized to its best-fit signal strength. The background histograms are stacked. The "others" background contribution includes events from diboson and single-top-quark production, as well as scalar boson decays to a pair of W bosons. The background uncertainty band accounts for all sources of background uncertainties, systematic as well as statistical, after the global fit.

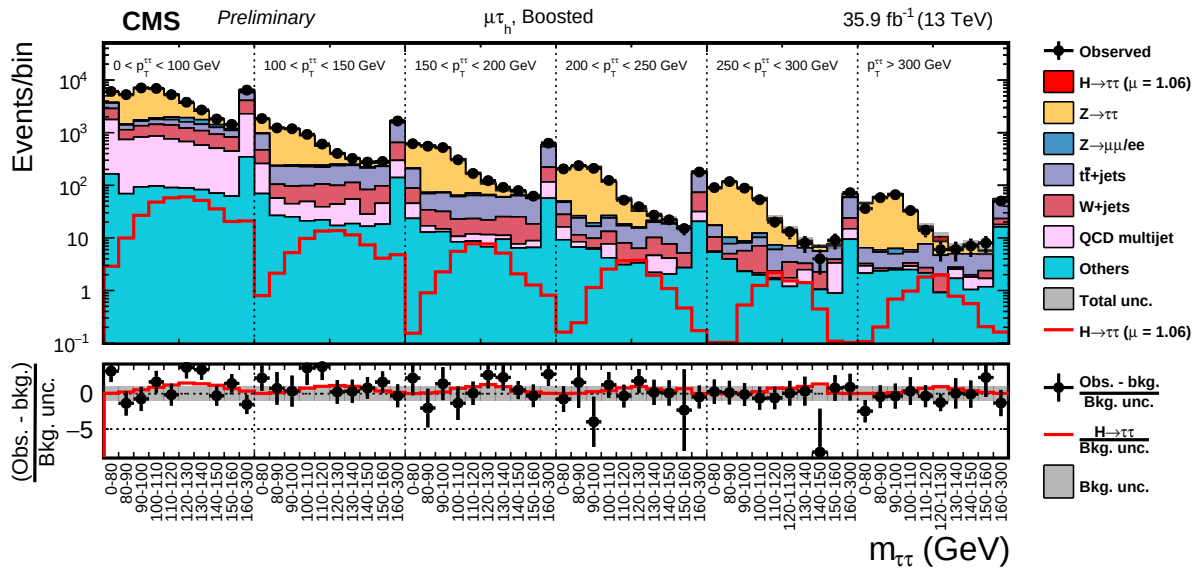

Figure 11: Observed and predicted 2D distributions in the boosted category of the $\mu\tau_h$ final state. The normalization of the predicted background distributions corresponds to the result of the global fit. The signal distribution is normalized to its best-fit signal strength. The background histograms are stacked. The "others" background contribution includes events from diboson and single-top-quark production, as well as scalar boson decays to a pair of W bosons. The background uncertainty band accounts for all sources of background uncertainties, systematic as well as statistical, after the global fit.

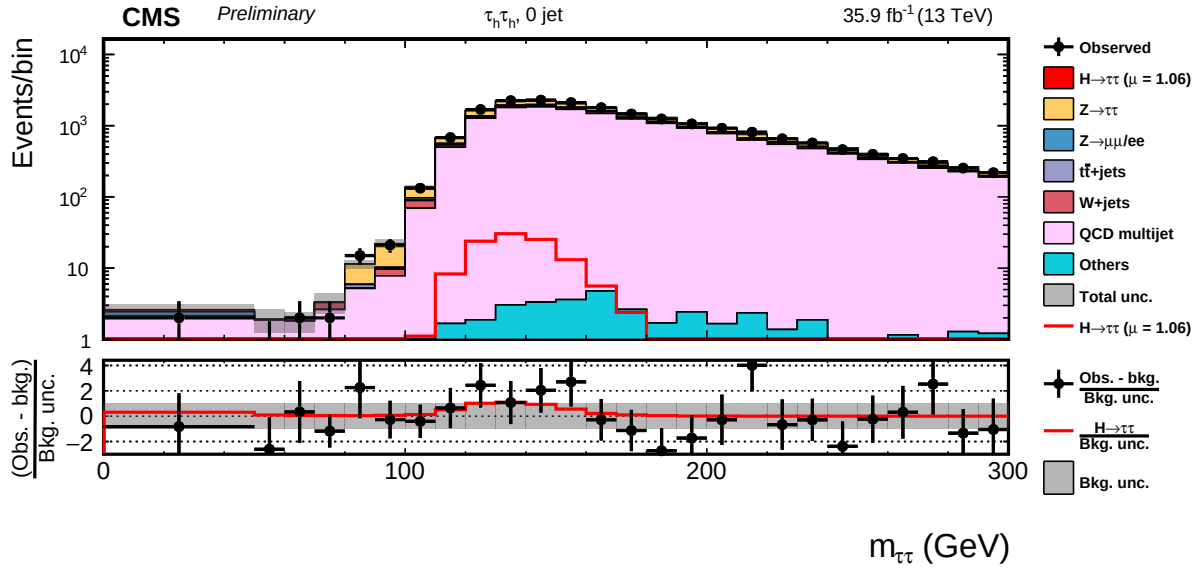

Figure 12: Observed and predicted 2D distributions in the 0-jet category of the $\tau_h\tau_h$ final state. The normalization of the predicted background distributions corresponds to the result of the global fit. The signal distribution is normalized to its best-fit signal strength. The background histograms are stacked. The "others" background contribution includes events from diboson and single-top-quark production, as well as scalar boson decays to a pair of W bosons. The background uncertainty band accounts for all sources of background uncertainties, systematic as well as statistical, after the global fit.

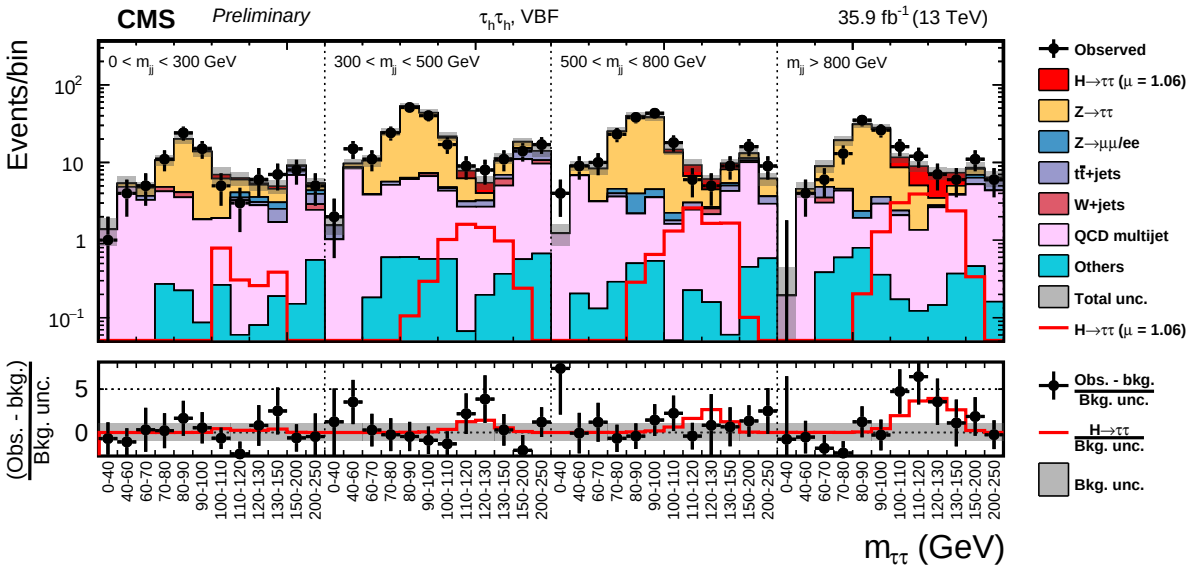

Figure 13: Observed and predicted 2D distributions in the VBF category of the $\tau_h\tau_h$ final state. The normalization of the predicted background distributions corresponds to the result of the global fit. The signal distribution is normalized to its best-fit signal strength. The background histograms are stacked. The "others" background contribution includes events from diboson and single-top-quark production, as well as scalar boson decays to a pair of W bosons. The background uncertainty band accounts for all sources of background uncertainties, systematic as well as statistical, after the global fit.

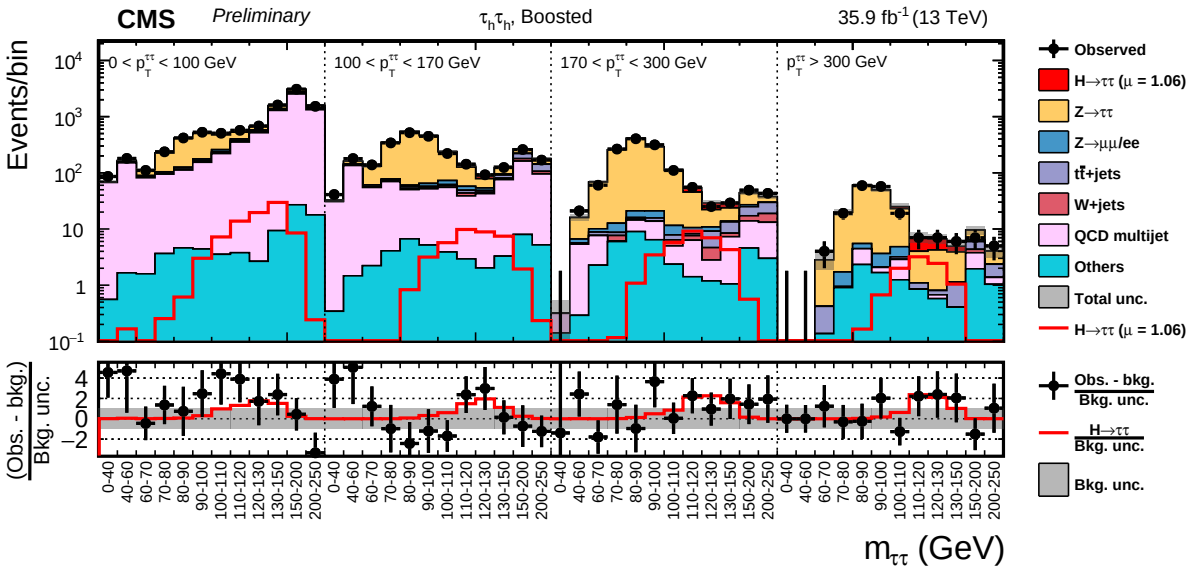

Figure 14: Observed and predicted 2D distributions in the boosted category of the $\tau_h\tau_h$ final state. The normalization of the predicted background distributions corresponds to the result of the global fit. The signal distribution is normalized to its best-fit signal strength. The background histograms are stacked. The "others" background contribution includes events from diboson and single-top-quark production, as well as scalar boson decays to a pair of W bosons. The background uncertainty band accounts for all sources of background uncertainties, systematic as well as statistical, after the global fit.

fit according to their probability density function. A log-normal probability density function is assumed for the nuisance parameters affecting the event yields of the various background contributions, whereas systematic uncertainties that affect the distributions are represented by nuisance parameters whose variation results in a continuous perturbation of the spectrum [81] and which are assumed to have a Gaussian probability density function. Overall, the statistical uncertainty in the observed event yields is the dominant source of uncertainty for all combined results.

The signal region events are rearranged in a histogram based on the the decimal logarithm of the ratio of the signal to signal-plus-background in each bin of the individual distributions used to extract the results. The resulting distribution is shown in Fig. 15. An excess of observed events with respect to the SM background expectation is clearly visible in the most sensitive bins of the analysis. The expected background and signal contributions, as well as the observed number of events, are indicated per process and category in Tab. 4 for the bins with $\log(S/(S+B)) > -0.9$. The channel that contributes the most to these bins is $\tau_h\tau_h$.

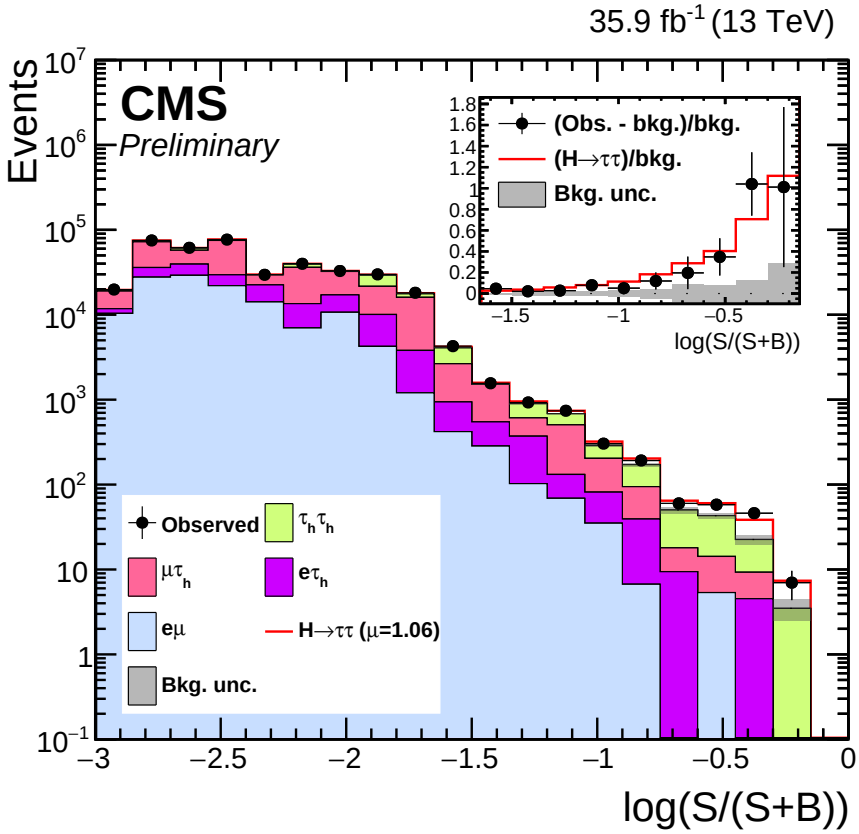

Figure 15: Distribution of the decimal logarithm of the ratio between the expected signal and the sum of expected signal and expected background in each bin of the mass distributions used to extract the results, in all signal regions. The background contributions are separated by decay channel. The inset shows the corresponding difference between the observed data and expected background distributions divided by the background expectation, as well as the signal expectation divided by the background expectation.

The excess of observed events relative to the background expectation is also visible in Fig. 16, where every mass distribution for a constant range of the second dimension of the signal distri-

Process	$e\mu$	$e\tau_h$	$\mu\tau_h$	$\tau_h\tau_h$
$Z \to \tau\tau$	5.77± 2.22	21.16± 3.28	34.57± 4.87	89.05± 6.91
$Z \to ee/\mu\mu$	0.00± 0.00	2.94± 0.18	3.66± 0.22	4.96± 0.24
$t\bar{t}$+jets	1.93± 0.09	10.38± 0.29	22.22± 1.79	13.91± 0.51
W+jets	0.81± 0.02	4.03± 0.30	6.59± 1.28	7.56± 0.81
QCD multijet	2.12± 0.25	3.33± 2.50	5.00± 1.27	35.50± 2.08
Other bkg.	1.44± 0.04	5.19± 0.20	6.05± 0.21	7.25± 0.20
$gg \to H, H \to \tau\tau$	0.58± 0.09	5.00± 0.55	6.01± 0.58	27.38± 2.09
$qq \to H, H \to \tau\tau$	2.78± 0.30	5.14± 0.47	12.55± 1.02	17.50± 1.04
$VH, H \to \tau\tau$	0.00± 0.00	0.29± 0.03	0.24± 0.03	1.34± 0.10
Total bkg.	12.05± 2.16	46.53± 4.10	77.66± 5.50	156.16± 7.34
Total signal	3.37± 0.36	10.92± 0.79	19.24± 1.39	48.29± 2.63
Observed	11	54	91	207

Table 4: Background and signal expectations, together with the number of observed events, in the signal region bins that have $\log(S/(S+B)) > -0.9$, where S and B are, respectively, the number of expected signal and background events in those bins. The background uncertainty accounts for all sources of background uncertainties, systematic as well as statistical, after the global fit. The contribution from "other backgrounds" includes events from diboson and single-top-quark production, as well as scalar boson decays to a pair of W bosons.

butions has been added up with a weight $S/(S+B)$ in order to increase the contribution of the most sensitive distributions. In this case, S and B are computed, respectively, as the signal or background contribution in the mass distribution excluding the first and last bins, in which the amount of signal is negligible. The signal regions that use m_{vis} instead of $m_{\tau\tau}$, namely the 0-jet category of the $e\mu$, $e\tau_h$ and $\mu\tau_h$ channels, are not included. The right figure includes the VBF category of the $e\mu$, $e\tau_h$ and $\mu\tau_h$ channels, and is separated from the left figure, which includes all other distributions, because of incompatible binnings.

The excess in data is quantified by calculating the corresponding local p-values using a profile-likelihood ratio test statistics [82, 83]. As shown in Fig. 17, the observed significance for a SM scalar boson with $m_H = 125\,\text{GeV}$ is 4.9 standard deviations, for an expected significance of 4.7 standard deviations.

The corresponding best-fit value for the signal strength μ is $\hat{\mu} = 1.06 \pm 0.25$ at $m_H = 125\,\text{GeV}$. The uncertainty on the best-fit signal strength can be decomposed into four components: theory uncertainties, bin-by-bin statistical uncertainties on the backgrounds, other systematic uncertainties, and statistical uncertainty. In that format, the best-fit signal strength is $\hat{\mu} = 1.06^{+0.11}_{-0.09}$ (th.) $^{+0.12}_{-0.12}$ (bbb.) $^{+0.13}_{-0.12}$ (syst.) $^{+0.15}_{-0.15}$ (stat.). The individual best-fit signal strengths per channel and per category are given in Fig. 18; they demonstrate the channel- and category-wise consistency of the observation with the SM scalar boson hypothesis.

A likelihood scan is performed for $m_H = 125\,\text{GeV}$ in the (κ_V,κ_f) parameter space, where κ_V and κ_f quantify, respectively, the ratio between the measured and the SM value for the couplings of the scalar boson to vector bosons and fermions. For this scan, scalar boson decays to pairs of W bosons are considered as part of the signal. All nuisance parameters are profiled for each point of the scan. As shown in Fig. 19, the observed likelihood contour is consistent with the SM expectation of κ_V and κ_f equal to unity.

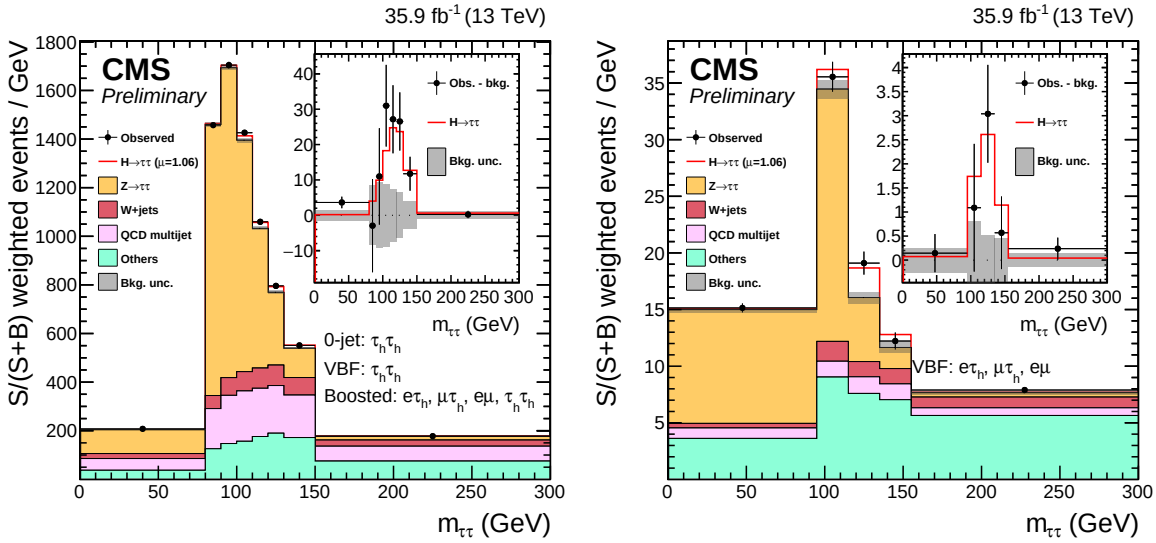

Figure 16: Combined observed and predicted $m_{\tau\tau}$ distributions. The right figure includes the VBF category of the eμ, eτ_h and $\mu\tau_h$ channels, and the left figure includes all other channels that make use of $m_{\tau\tau}$ and not m_{vis}. The normalization of the predicted background distributions corresponds to the result of the global fit, while the signal is normalized to its best-fit signal strength. The mass distribution for a constant range of the second dimension of the signal distributions are weighted according to $S/(S+B)$, where S and B are computed, respectively, as the signal or background contribution in the mass distribution excluding the first and last bins. The "others" background contribution includes events from diboson, $t\bar{t}$, and single-top-quark production, as well as scalar boson decays to a pair of W bosons and Z bosons decaying to a pair of light leptons. The background uncertainty band accounts for all sources of background uncertainties, systematic as well as statistical, after the global fit. The inset shows the corresponding difference between the observed data and expected background distributions, together with the signal expectation. The signal normalization is equal to its normalization before reweighting.

10 Summary

A search for the SM scalar boson based on data collected in pp collisions by the CMS detector in 2016 at a center-of-mass energy of 13 TeV, has been presented. The four di-τ final states with the largest branching fraction have been studied, in event categories targeting Higgs boson signal events produced via gluon-gluon fusion and vector boson fusion. The results are extracted via two-dimensional maximum likelihood fits in the planes defined by the full or visible di-τ mass, and the lepton transverse momentum or τ_h reconstructed decay mode in the 0-jet category, the invariant mass of the di-jets in the VBF category, and the scalar boson candidate transverse momentum in the boosted category. This leads to the observation of decays of the SM scalar boson to pairs of τ leptons, with an observed significance of 4.9 standard deviations for a mass of 125 GeV. This is to be compared with an expected significance of 4.7 standard deviations.

References

[1] S. Weinberg, "A Model of Leptons", *Phys. Rev. Lett.* **19** (1967) 1264, doi:10.1103/PhysRevLett.19.1264.

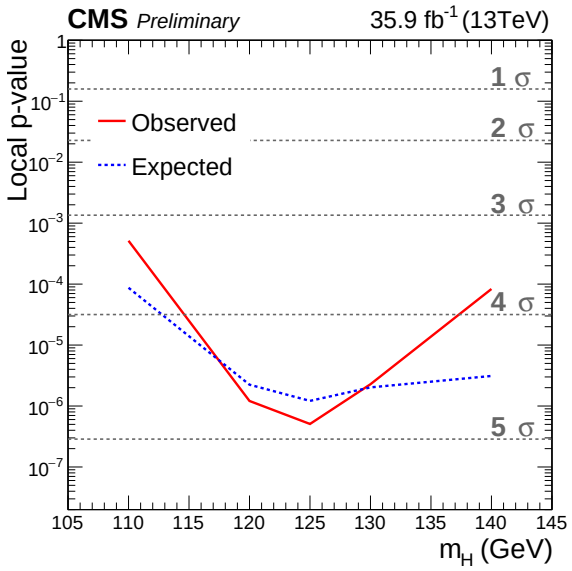

Figure 17: Local p-value and significance as a function of the SM scalar boson mass hypothesis. The observation (black) is compared to the expectation (blue) for a scalar boson with a mass $m_{\mathrm{H}} = 125\,\mathrm{GeV}$. The background includes scalar boson decays to a pair of W bosons, with $m_{\mathrm{H}} = 125\,\mathrm{GeV}$.

[2] A. Salam, "Weak and electromagnetic interactions", in *Elementary particle physics: relativistic groups and analyticity*, N. Svartholm, ed., p. 367. Almqvist & Wiksell, Stockholm, 1968. Proceedings of the eighth Nobel symposium.

[3] F. Englert and R. Brout, "Broken Symmetry and the Mass of Gauge Vector Mesons", *Phys. Rev. Lett.* **13** (1964) 321, doi:10.1103/PhysRevLett.13.321.

[4] P. W. Higgs, "Broken symmetries, massless particles and gauge fields", *Phys. Lett.* **12** (1964) 132, doi:10.1016/0031-9163(64)91136-9.

[5] P. W. Higgs, "Broken Symmetries and the Masses of Gauge Bosons", *Phys. Rev. Lett.* **13** (1964) 508, doi:10.1103/PhysRevLett.13.508.

[6] G. S. Guralnik, C. R. Hagen, and T. W. B. Kibble, "Global Conservation Laws and Massless Particles", *Phys. Rev. Lett.* **13** (1964) 585, doi:10.1103/PhysRevLett.13.585.

[7] P. W. Higgs, "Spontaneous Symmetry Breakdown without Massless Bosons", *Phys. Rev.* **145** (1966) 1156, doi:10.1103/PhysRev.145.1156.

[8] T. W. B. Kibble, "Symmetry Breaking in Non-Abelian Gauge Theories", *Phys. Rev.* **155** (1967) 1554, doi:10.1103/PhysRev.155.1554.

[9] ATLAS Collaboration, "Observation of a new particle in the search for the Standard Model Higgs boson with the ATLAS detector at the LHC", *Phys. Lett. B* **716** (2012) 1, doi:10.1016/j.physletb.2012.08.020, arXiv:1207.7214.

[10] CMS Collaboration, "Observation of a new boson at a mass of 125 GeV with the CMS experiment at the LHC", *Phys. Lett. B* **716** (2012) 30, doi:10.1016/j.physletb.2012.08.021, arXiv:1207.7235.

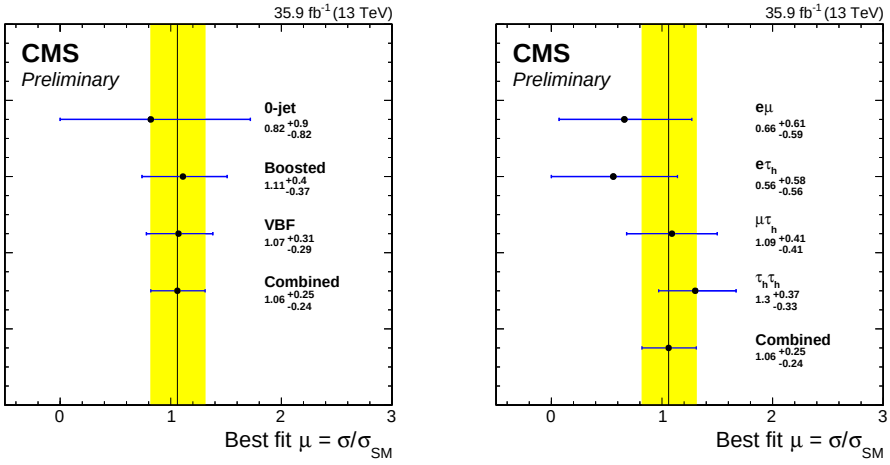

Figure 18: Best-fit signal strength per category (left) and channel (right), for $m_{\mathrm{H}} = 125\,\mathrm{GeV}$. The constraints from the global fit are used to extract each of the individual best-fit signal strengths. The combined best-fit signal strength is $\hat{\mu} = 1.06 \pm 0.25$.

[11] CMS Collaboration, "Observation of a new boson with mass near 125 GeV in pp collisions at $\sqrt{s}$ = 7 and 8 TeV", *JHEP* **06** (2013) 081, doi:10.1007/JHEP06(2013)081, arXiv:1303.4571.

[12] ATLAS Collaboration, "Measurements of the Higgs boson production and decay rates and coupling strengths using pp collision data at $\sqrt{s} = 7$ and 8 TeV in the ATLAS experiment", *Eur. Phys. J. C* **76** (2016) 6, doi:10.1140/epjc/s10052-015-3769-y, arXiv:1507.04548.

[13] CMS Collaboration, "Precise determination of the mass of the Higgs boson and tests of compatibility of its couplings with the standard model predictions using proton collisions at 7 and 8 TeV", *Eur. Phys. J. C* **75** (2015), no. 5, 212, doi:10.1140/epjc/s10052-015-3351-7, arXiv:1412.8662.

[14] CMS Collaboration, "Study of the Mass and Spin-Parity of the Higgs Boson Candidate Via Its Decays to Z Boson Pairs", *Phys. Rev. Lett.* **110** (2013), no. 8, 081803, doi:10.1103/PhysRevLett.110.081803, arXiv:1212.6639.

[15] ATLAS Collaboration, "Evidence for the spin-0 nature of the Higgs boson using ATLAS data", *Phys. Lett. B* **726** (2013) 120, doi:10.1016/j.physletb.2013.08.026, arXiv:1307.1432.

[16] CMS Collaboration, "Constraints on the spin-parity and anomalous HVV couplings of the Higgs boson in proton collisions at 7 and 8 TeV", *Phys. Rev. D* **92** (2015) 012004, doi:10.1103/PhysRevD.92.012004, arXiv:1411.3441.

[17] ATLAS, CMS Collaboration, "Combined Measurement of the Higgs Boson Mass in pp Collisions at $\sqrt{s} = 7$ and 8 TeV with the ATLAS and CMS Experiments", *Phys. Rev. Lett.* **114** (2015) 191803, doi:10.1103/PhysRevLett.114.191803, arXiv:1503.07589.

[18] ALEPH Collaboration, "Observation of an excess in the search for the Standard Model Higgs boson at ALEPH", *Phys. Lett. B* **495** (2000) 1, doi:10.1016/S0370-2693(00)01269-7, arXiv:hep-ex/0011045.

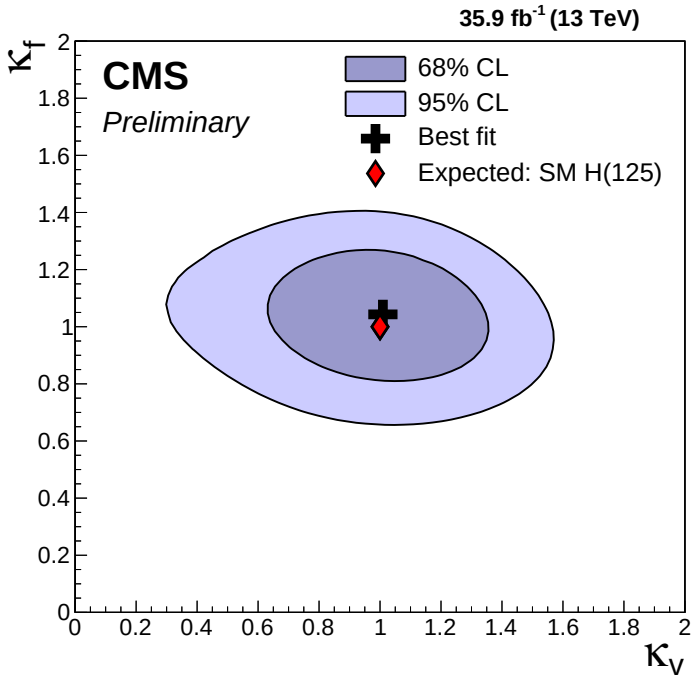

Figure 19: Scan of the negative log-likelihood difference as a function of κ_V and κ_f, for $m_{\mathrm{H}} = 125\,\mathrm{GeV}$. All nuisance parameters are profiled for each point. For this scan, the $pp \to H(125\ \mathrm{GeV}) \to WW$ contribution is treated as a signal process.

[19] DELPHI Collaboration, "Final results from DELPHI on the searches for SM and MSSM neutral Higgs bosons", *Eur. Phys. J. C* **32** (2004) 145, doi:10.1140/epjc/s2003-01394-x, arXiv:hep-ex/0303013.

[20] L3 Collaboration, "Standard model Higgs boson with the L3 experiment at LEP", *Phys. Lett. B* **517** (2001) 319, doi:10.1016/S0370-2693(01)01010-3, arXiv:hep-ex/0107054.

[21] OPAL Collaboration, "Search for the Standard Model Higgs boson in e^+e^- collisions at $\sqrt{s}$ = 192–209 GeV", *Phys. Lett. B* **499** (2001) 38, doi:10.1016/S0370-2693(01)00070-3, arXiv:hep-ex/0101014.

[22] CDF Collaboration, "Search for a Low-Mass Standard Model Higgs Boson in the $\tau\tau$ Decay Channel in $p\bar{p}$ Collisions at $\sqrt{s}$ = 1.96 TeV", *Phys. Rev. Lett.* **108** (2012) 181804, doi:10.1103/PhysRevLett.108.181804, arXiv:1201.4880.

[23] D0 Collaboration, "Search for the standard model Higgs boson in tau lepton final states", *Phys. Lett. B* **714** (2012) 237, doi:10.1016/j.physletb.2012.07.012, arXiv:1203.4443.

[24] ATLAS Collaboration, "Evidence for the Higgs-boson Yukawa coupling to tau leptons with the ATLAS detector", *JHEP* **04** (2015) 117, doi:10.1007/JHEP04(2015)117, arXiv:1501.04943.

[25] CMS Collaboration, "Evidence for the 125 GeV Higgs boson decaying to a pair of τ leptons", *JHEP* **05** (2014) 104, doi:10.1007/JHEP05(2014)104, arXiv:1401.5041.

[26] ATLAS, CMS Collaboration, "Measurements of the Higgs boson production and decay rates and constraints on its couplings from a combined ATLAS and CMS analysis of the LHC pp collision data at $\sqrt{s} = 7$ and 8 TeV", *JHEP* **08** (2016) 045, doi:10.1007/JHEP08(2016)045, arXiv:1606.02266.

[27] CMS Collaboration, "The CMS trigger system", (2016). arXiv:1609.02366.

[28] CMS Collaboration, "The CMS experiment at the CERN LHC", *JINST* **3** (2008) S08004, doi:10.1088/1748-0221/3/08/S08004.

[29] P. Nason, "A new method for combining NLO QCD with shower Monte Carlo algorithms", *JHEP* **11** (2004) 040, doi:10.1088/1126-6708/2004/11/040, arXiv:hep-ph/0409146.

[30] S. Frixione, P. Nason, and C. Oleari, "Matching NLO QCD computations with parton shower simulations: the POWHEG method", *JHEP* **11** (2007) 070, doi:10.1088/1126-6708/2007/11/070, arXiv:0709.2092.

[31] S. Alioli, P. Nason, C. Oleari, and E. Re, "A general framework for implementing NLO calculations in shower Monte Carlo programs: the POWHEG BOX", *JHEP* **06** (2010) 043, doi:10.1007/JHEP06(2010)043, arXiv:1002.2581.

[32] S. Alioli et al., "Jet pair production in POWHEG", *JHEP* **04** (2011) 081, doi:10.1007/JHEP04(2011)081, arXiv:1012.3380.

[33] S. Alioli, P. Nason, C. Oleari, and E. Re, "NLO Higgs boson production via gluon fusion matched with shower in POWHEG", *JHEP* **04** (2009) 002, doi:10.1088/1126-6708/2009/04/002, arXiv:0812.0578.

[34] J. Alwall et al., "MadGraph 5: going beyond", *JHEP* **06** (2011) 128, doi:10.1007/JHEP06(2011)128, arXiv:1106.0522.

[35] J. Alwall et al., "The automated computation of tree-level and next-to-leading order differential cross sections, and their matching to parton shower simulations", *JHEP* **07** (2014) 079, doi:10.1007/JHEP07(2014)079, arXiv:1405.0301.

[36] CMS Collaboration, "Event generator tunes obtained from underlying event and multiparton scattering measurements", *Eur. Phys. J. C* **76** (2016), no. 3, 155, doi:10.1140/epjc/s10052-016-3988-x, arXiv:1512.00815.

[37] LHC Higgs Cross Section Working Group, "Handbook of LHC Higgs cross sections: 1. Inclusive observables", CERN Report CERN-2011-002, 2011. doi:10.5170/CERN-2011-002, arXiv:1101.0593.

[38] LHC Higgs Cross Section Working Group, "Handbook of LHC Higgs cross sections: 2. Differential Distributions", CERN Report CERN-2012-002, 2012. doi:10.5170/CERN-2012-002, arXiv:1201.3084.

[39] LHC Higgs Cross Section Working Group, "Handbook of LHC Higgs cross sections: 3. Higgs Properties", CERN Report CERN-2013-004, 2013. doi:10.5170/CERN-2013-004, arXiv:1307.1347.

[40] A. Djouadi, M. Spira, and P. M. Zerwas, "Production of Higgs bosons in proton colliders. QCD corrections", *Phys. Lett. B* **264** (1991) 440, doi:10.1016/0370-2693(91)90375-Z.

[41] S. Dawson, "Radiative corrections to Higgs boson production", *Nucl. Phys. B* **359** (1991) 283, doi:10.1016/0550-3213(91)90061-2.

[42] M. Spira, A. Djouadi, D. Graudenz, and P. M. Zerwas, "Higgs boson production at the LHC", *Nucl. Phys. B* **453** (1995) 17, doi:10.1016/0550-3213(95)00379-7, arXiv:hep-ph/9504378.

[43] R. V. Harlander and W. B. Kilgore, "Next-to-Next-to-Leading Order Higgs Production at Hadron Colliders", *Phys. Rev. Lett.* **88** (2002) 201801, doi:10.1103/PhysRevLett.88.201801, arXiv:hep-ph/0201206.

[44] C. Anastasiou and K. Melnikov, "Higgs boson production at hadron colliders in NNLO QCD", *Nucl. Phys. B* **646** (2002) 220, doi:10.1016/S0550-3213(02)00837-4, arXiv:hep-ph/0207004.

[45] V. Ravindran, J. Smith, and W. L. van Neerven, "NNLO corrections to the total cross section for Higgs boson production in hadron-hadron collisions", *Nucl. Phys. B* **665** (2003) 325, doi:10.1016/S0550-3213(03)00457-7, arXiv:hep-ph/0302135.

[46] S. Catani, D. de Florian, M. Grazzini, and P. Nason, "Soft-gluon resummation for Higgs boson production at hadron colliders", *JHEP* **07** (2003) 028, doi:10.1088/1126-6708/2003/07/028.

[47] U. Aglietti, R. Bonciani, G. Degrassi, and A. Vicini, "Two-loop light fermion contribution to Higgs production and decays", *Phys. Lett. B* **595** (2004) 432, doi:10.1016/j.physletb.2004.06.063, arXiv:hep-ph/0404071.

[48] G. Degrassi and F. Maltoni, "Two-loop electroweak corrections to Higgs production at hadron colliders", *Phys. Lett. B* **600** (2004) 255, doi:10.1016/j.physletb.2004.09.008, arXiv:hep-ph/0407249.

[49] S. Actis, G. Passarino, C. Sturm, and S. Uccirati, "NLO electroweak corrections to Higgs boson production at hadron colliders", *Phys. Lett. B* **670** (2008) 12, doi:10.1016/j.physletb.2008.10.018, arXiv:0809.1301.

[50] C. Anastasiou, R. Boughezal, and F. Petriello, "Mixed QCD-electroweak corrections to Higgs boson production in gluon fusion", *JHEP* **04** (2009) 003, doi:10.1088/1126-6708/2009/04/003, arXiv:0811.3458.

[51] D. de Florian and M. Grazzini, "Higgs production through gluon fusion: Updated cross sections at the Tevatron and the LHC", *Phys. Lett. B* **674** (2009) 291, doi:10.1016/j.physletb.2009.03.033, arXiv:0901.2427.

[52] J. Baglio and A. Djouadi, "Higgs production at the LHC", *JHEP* **03** (2011) 055, doi:10.1007/JHEP03(2011)055, arXiv:1012.0530.

[53] M. Ciccolini, A. Denner, and S. Dittmaier, "Strong and Electroweak Corrections to the Production of a Higgs Boson + 2 Jets via Weak Interactions at the Large Hadron Collider", *Phys. Rev. Lett.* **99** (2007) 161803, doi:10.1103/PhysRevLett.99.161803, arXiv:0707.0381.

[54] M. Ciccolini, A. Denner, and S. Dittmaier, "Electroweak and QCD corrections to Higgs production via vector-boson fusion at the CERN LHC", *Phys. Rev. D* **77** (2008) 013002, doi:10.1103/PhysRevD.77.013002, arXiv:0710.4749.

[55] K. Arnold et al., "VBFNLO: A parton level Monte Carlo for processes with electroweak bosons", *Comput. Phys. Commun.* **180** (2009) 1661, doi:10.1016/j.cpc.2009.03.006, arXiv:0811.4559.

[56] O. Brein, A. Djouadi, and R. Harlander, "NNLO QCD corrections to the Higgs-strahlung processes at hadron colliders", *Phys. Lett. B* **579** (2004) 149, doi:10.1016/j.physletb.2003.10.112, arXiv:hep-ph/0307206.

[57] M. L. Ciccolini, S. Dittmaier, and M. Krämer, "Electroweak radiative corrections to associated WH and ZH production at hadron colliders", *Phys. Rev. D* **68** (2003) 073003, doi:10.1103/PhysRevD.68.073003, arXiv:hep-ph/0306234.

[58] A. Djouadi, J. Kalinowski, M. Muhlleitner, and M. Spira, "An update of the program HDECAY", in *The Les Houches 2009 workshop on TeV colliders: The tools and Monte Carlo working group summary report*. 2010. arXiv:1003.1643.

[59] A. Denner et al., "Standard model Higgs-boson branching ratios with uncertainties", *Eur. Phys. J. C* **71** (2011) 1753, doi:10.1140/epjc/s10052-011-1753-8, arXiv:1107.5909.

[60] S. Alekhin et al., "The PDF4LHC Working Group Interim Report", (2011). arXiv:1101.0536.

[61] M. Botje et al., "The PDF4LHC Working Group Interim Recommendations", (2011). arXiv:1101.0538.

[62] H.-L. Lai et al., "New parton distributions for collider physics", *Phys. Rev. D* **82** (2010) 074024, doi:10.1103/PhysRevD.82.074024, arXiv:1007.2241.

[63] NNPDF Collaboration, "Impact of heavy quark masses on parton distributions and LHC phenomenology", *Nucl. Phys. B* **849** (2011) 296, doi:10.1016/j.nuclphysb.2011.03.021, arXiv:1101.1300.

[64] LHC Higgs Cross Section Working Group Collaboration, "Handbook of LHC Higgs Cross Sections: 4. Deciphering the Nature of the Higgs Sector", arXiv:1610.07922.

[65] GEANT4 Collaboration, "GEANT4 — a simulation toolkit", *Nucl. Instrum. Meth. A* **506** (2003) 250, doi:10.1016/S0168-9002(03)01368-8.

[66] CMS Collaboration, "Particle–Flow Event Reconstruction in CMS and Performance for Jets, Taus, and $E_{\mathrm{T}}^{\mathrm{miss}}$", CMS Physics Analysis Summary CMS-PAS-PFT-09-001, 2009.

[67] CMS Collaboration, "Commissioning of the Particle-Flow Reconstruction in Minimum-Bias and Jet Events from pp Collisions at 7 TeV", CMS Physics Analysis Summary CMS-PAS-PFT-10-002, 2010.

[68] CMS Collaboration, "Commissioning of the particle-flow event reconstruction with leptons from J/Ψ and W decays at 7 TeV", CMS Physics Analysis Summary CMS-PAS-PFT-10-003, 2010.

[69] CMS Collaboration, "Performance of CMS muon reconstruction in pp collision events at $\sqrt{s} = 7$ TeV", *JINST* **7** (2012) P10002, doi:10.1088/1748-0221/7/10/P10002, arXiv:1206.4071.

[70] CMS Collaboration, "Electron Reconstruction and Identification at $\sqrt{s} = 7$ TeV", CMS Physics Analysis Summary CMS-PAS-EGM-10-004, 2010.

[71] M. Cacciari, G. P. Salam, and G. Soyez, "FastJet user manual", *Eur. Phys. J. C* **72** (2012) 1896, doi:10.1140/epjc/s10052-012-1896-2, arXiv:1111.6097.

[72] M. Cacciari and G. P. Salam, "Dispelling the N^3 myth for the k_t jet-finder", *Phys. Lett. B* **641** (2006) 57, doi:10.1016/j.physletb.2006.08.037, arXiv:hep-ph/0512210.

[73] CMS Collaboration, "Determination of jet energy calibration and transverse momentum resolution in CMS", *JINST* **6** (2011) 11002, doi:10.1088/1748-0221/6/11/P11002, arXiv:1107.4277.

[74] CMS Collaboration, "Reconstruction and identification of τ lepton decays to hadrons and ν_τ at CMS", *JINST* **11** (2016) P01019, doi:10.1088/1748-0221/11/01/P01019, arXiv:1510.07488.

[75] CMS Collaboration, "Performance of reconstruction and identification of tau leptons in their decays to hadrons and tau neutrino in LHC Run-2", (2016).

[76] H. Voss, A. Höcker, J. Stelzer, and F. Tegenfeldt, "TMVA, the Toolkit for Multivariate Data Analysis with ROOT", in *XI Int. Workshop on Advanced Computing and Analysis Techniques in Physics Research*. 2007. arXiv:physics/0703039. PoS ACAT:040.

[77] CMS Collaboration, "Performance of Missing Transverse Momentum Reconstruction Algorithms in Proton-Proton Collisions at $\sqrt{s} = 8$ TeV with the CMS Detector", CMS Physics Analysis Summary CMS-PAS-JME-12-002, 2012.

[78] L. Bianchini, J. Conway, E. K. Friis, and C. Veelken, "Reconstruction of the Higgs mass in $H \to \tau\tau$ Events by Dynamical Likelihood techniques", *J. Phys. Conf. Ser.* **513** (2014) 022035, doi:10.1088/1742-6596/513/2/022035.

[79] D. de Florian, G. Ferrera, M. Grazzini, and D. Tommasini, "Higgs boson production at the LHC: transverse momentum resummation effects in the H $\to \gamma\gamma$, H $\to WW \to l\nu l\nu$ and H $\to ZZ \to 4l$ decay modes", *JHEP* **06** (2012) 132, doi:10.1007/JHEP06(2012)132, arXiv:1203.6321.

[80] M. Grazzini and H. Sargsyan, "Heavy-quark mass effects in Higgs boson production at the LHC", *JHEP* **09** (2013) 129, doi:10.1007/JHEP09(2013)129, arXiv:1306.4581.

[81] J. S. Conway, "Incorporating Nuisance Parameters in Likelihoods for Multisource Spectra", in *Proceedings of PHYSTAT 2011 Workshop on Statistical Issues Related to Discovery Claims in Search Experiments and Unfolding*, p. 115. CERN-2011-006, 2011.

[82] ATLAS and CMS Collaborations, LHC Higgs Combination Group, "Procedure for the LHC Higgs boson search combination in Summer 2011", Technical Report ATL-PHYS-PUB 2011-11, CMS NOTE 2011/005, CERN, 2011.

[83] CMS Collaboration, "Combined results of searches for the standard model Higgs boson in pp collisions at $\sqrt{s} = 7$ TeV", *Phys. Lett. B* **710** (2012) 26, doi:10.1016/j.physletb.2012.02.064, arXiv:1202.1488.

A Supplemental material

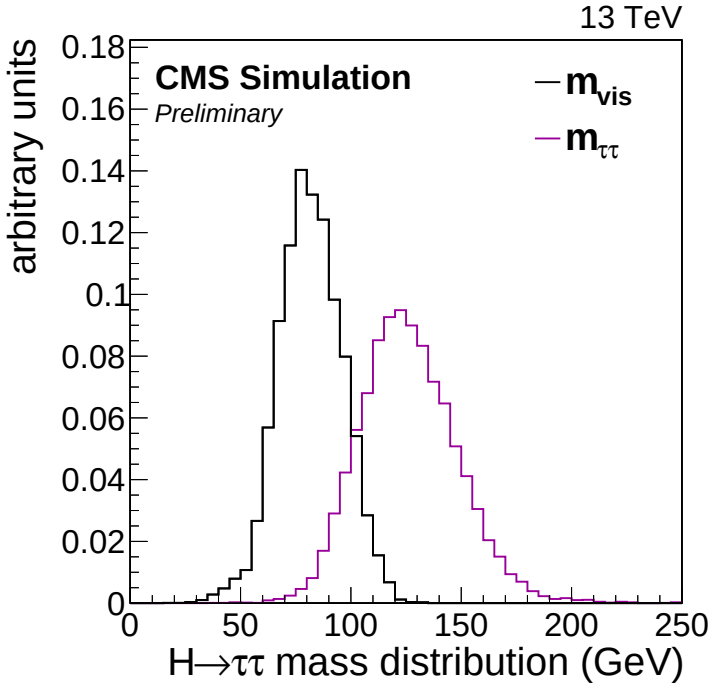

Figure 20: Normalized distributions of the visible mass, m_{vis}, and of the SVfit mass, $m_{\tau\tau}$, for a signal sample with a SM scalar boson of mass $m_{\text{H}} = 125$ GeV decaying to a pair of τ leptons in the $\mu\tau_{\text{h}}$ final state.

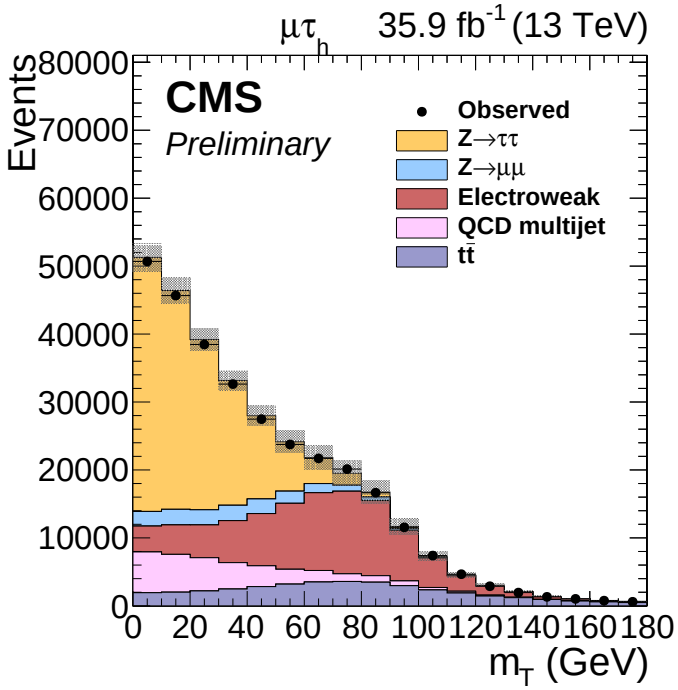

Figure 21: Observed and expected distributions of the transverse mass between the muon and $E_{\mathrm{T}}^{\mathrm{miss}}$, in the $\mu\tau_{\mathrm{h}}$ final state. The selection is inclusive in the number of jets. The background distributions have not been fitted to the data. The electroweak component of the background includes W+jets, single top quark, and diboson production events.

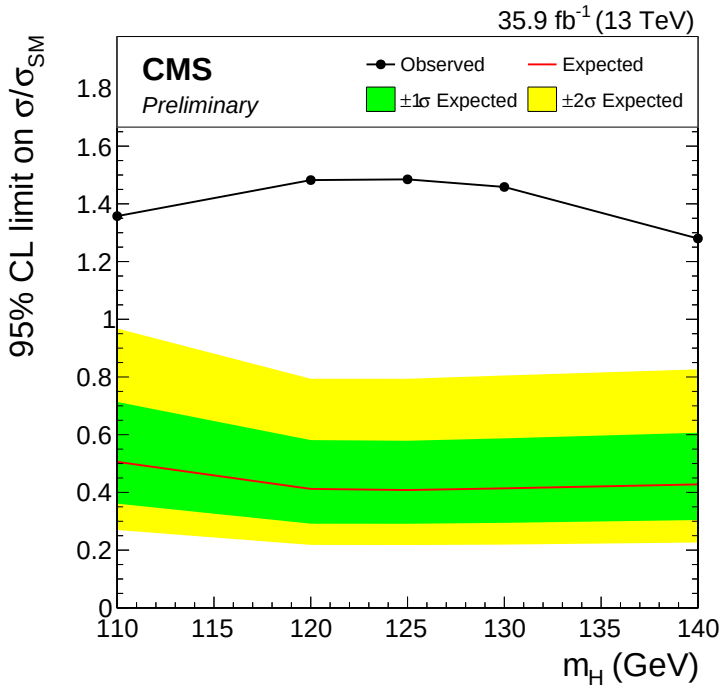

Figure 22: Combined observed 95% CL upper limit on the signal strength parameter μ, together with the expected limit obtained in the background-only hypothesis. The uncertainty bands show the expected one- and two-standard-deviation probability intervals around the expected limit. Scalar boson decays to pairs of W bosons are considered as a background.

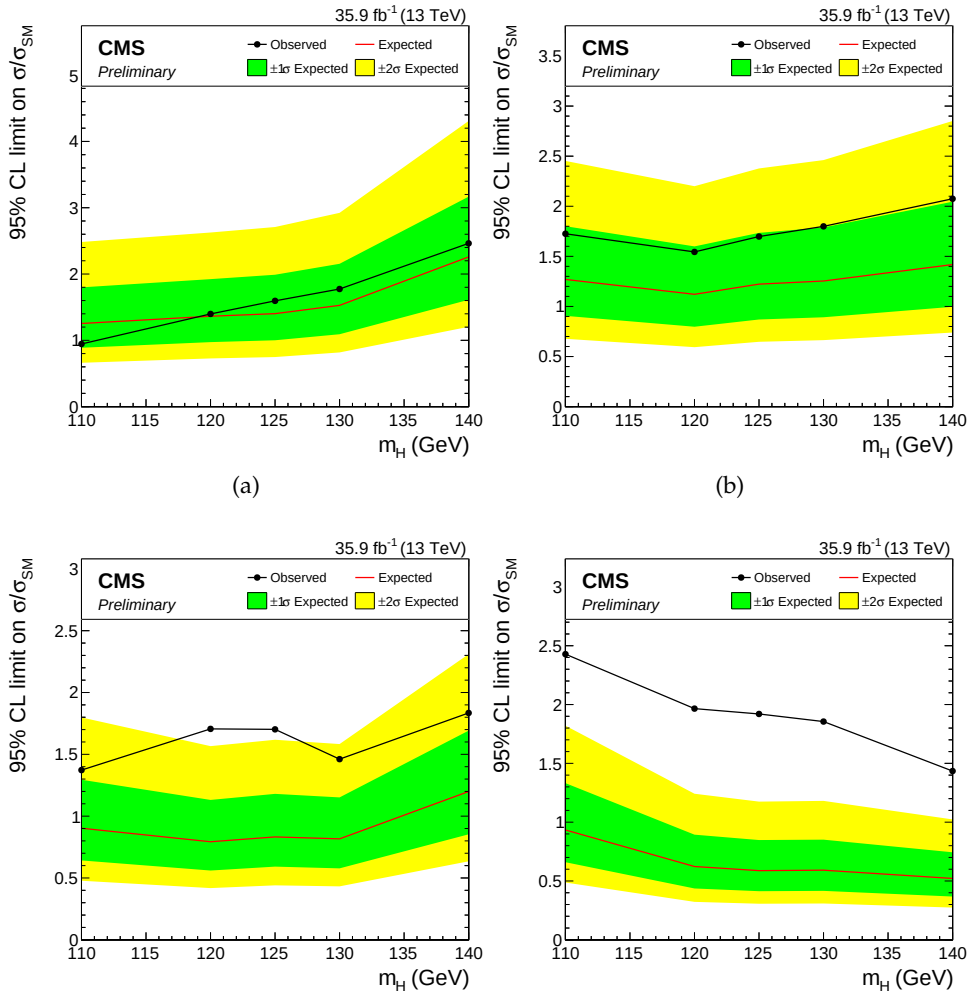

Figure 23: Observed 95% CL upper limit on the signal strength parameter μ, in the eμ (a), eτ_h (b), $\mu\tau_h$ (c), and $\tau_h\tau_h$ (d) final states, together with the expected limit obtained in the background-only hypothesis. The uncertainty bands show the expected one- and two-standard-deviation probability intervals around the expected limit. Scalar boson decays to pairs of W bosons are considered as a background.

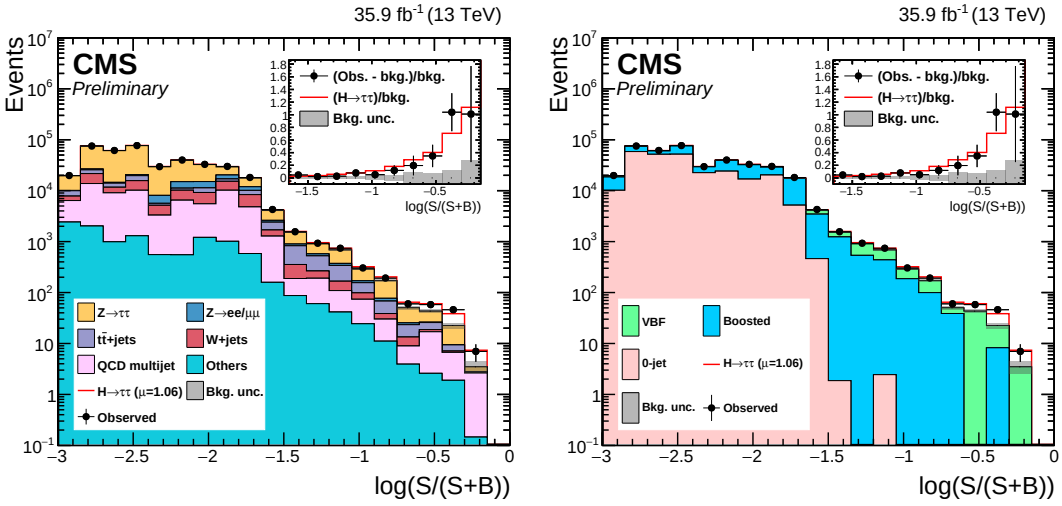

(a) (b)

Figure 24: Distribution of the decimal logarithm of the ratio between the expected signal and the sum of expected signal and expected background in each bin of the mass distributions used to extract the results, in all signal regions. The background contributions are separated by process (a) or by category (b). The inset shows the corresponding difference between the observed data and expected background distributions divided by the background expectation, as well as the signal expectation divided by the background expectation.

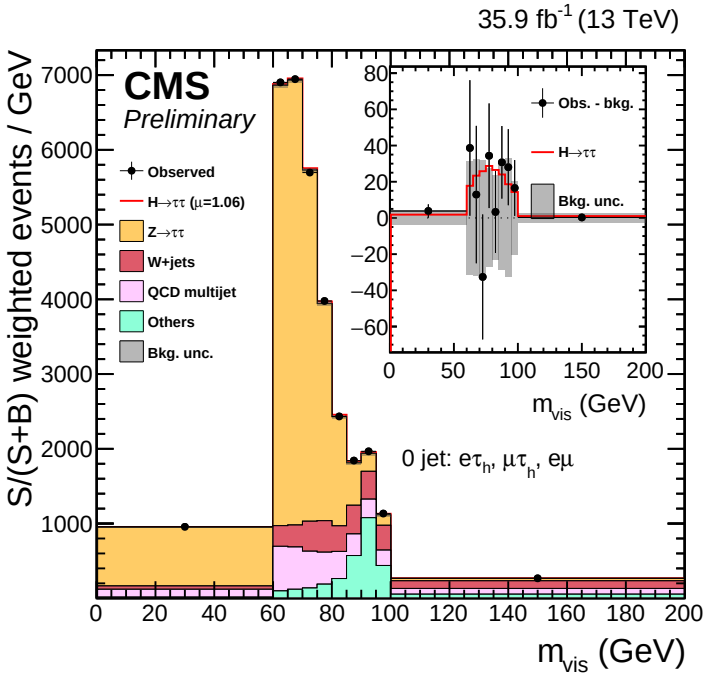

Figure 25: Combined observed and predicted m_{vis} distributions, in the 0-jet category of the eμ, eτ_{h}, and $\mu\tau_{\text{h}}$ channels. The normalization of the predicted background distributions corresponds to the result of the global fit, while the signal is normalized to its best-fit signal strength. The mass distributions for a constant range of the second dimension of the signal distributions are weighted according to $S/(S+B)$, where S and B are computed, respectively, as the signal or background contribution in the mass distribution excluding the first and last bins. The "others" background contribution includes events from diboson, $t\bar{t}$, and single-top-quark production, as well as scalar boson decays to a pair of W bosons and Z bosons decaying to a pair of light leptons. The background uncertainty band accounts for all sources of background uncertainties, systematic as well as statistical, after the global fit. The inset shows the corresponding difference between the observed data and expected background distributions, together with the signal expectation. The signal normalization after reweighting is equal to its normalization before reweighting, by construction.

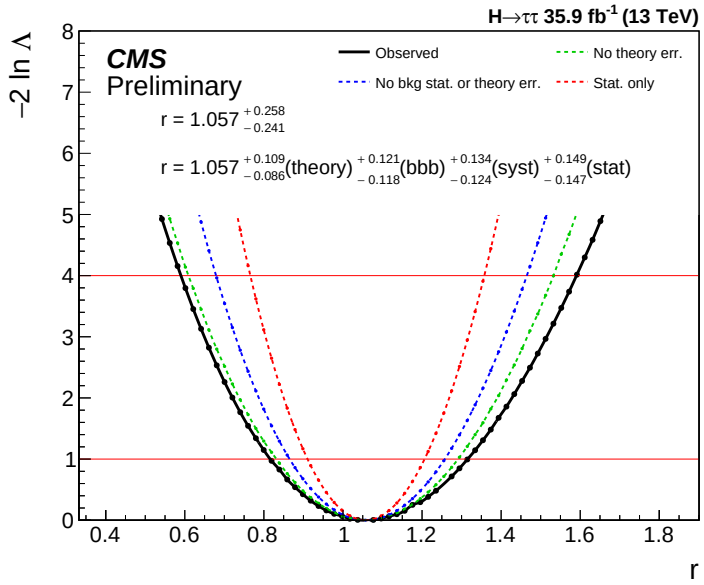

Figure 26: Profile likelihood ratio as a function of the signal strength parameter. The solid curve represents the observed profile likelihood ration. The green line is obtained by removing the theory-related uncertainties, the blue line by further removing the bin-by-bin background statistical uncertainties, and the red one by keeping only the statistical uncertainties.

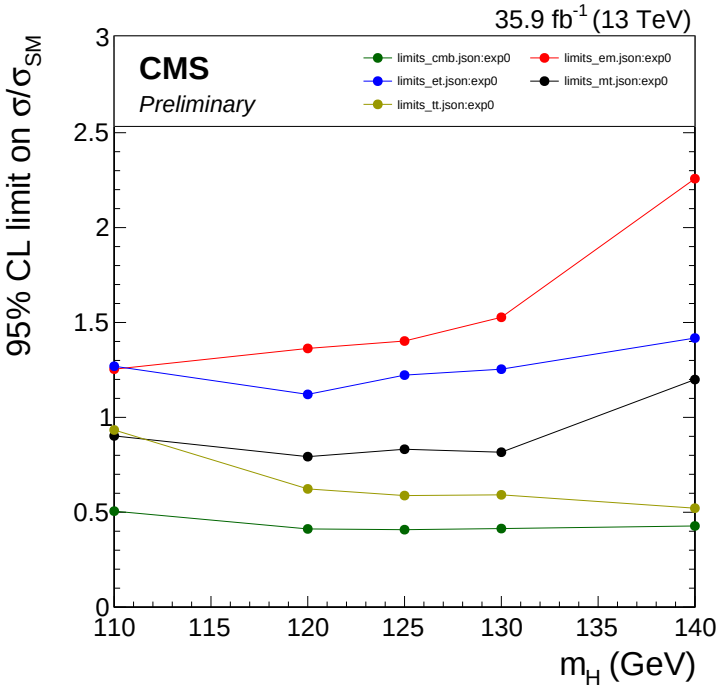

Figure 27: Expected 95% CL upper limits on the signal strength parameter for the eμ, eτ_h, $\mu\tau_h$, and $\tau_h\tau_h$ channels, together with the expected combined upper limit.

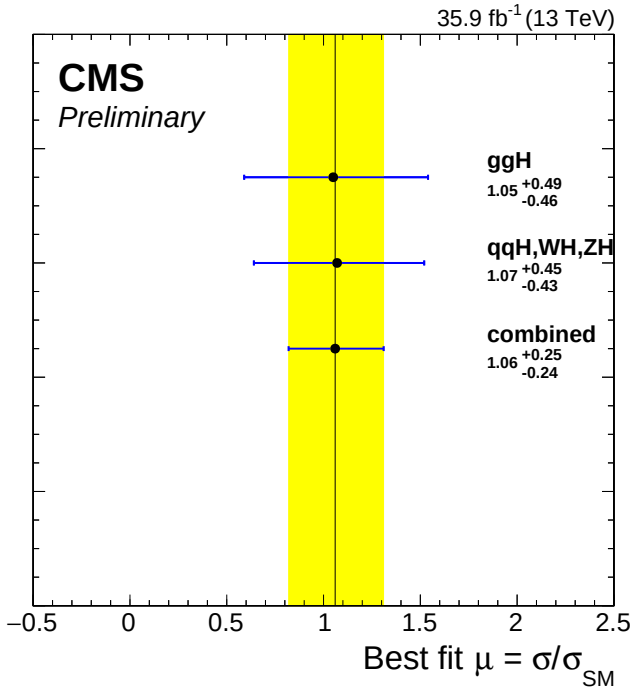

Figure 28: Best-fit signal strength for the ggH production, and for the other production modes, for $m_{\mathrm{H}} = 125\,\mathrm{GeV}$. The constraints from the global fit are used to extract each of the individual best-fit signal strengths. The combined best-fit signal strength is $\hat{\mu} = 1.06 \pm 0.25$.